



저작자표시-비영리-변경금지 2.0 대한민국

이용자는 아래의 조건을 따르는 경우에 한하여 자유롭게

- 이 저작물을 복제, 배포, 전송, 전시, 공연 및 방송할 수 있습니다.

다음과 같은 조건을 따라야 합니다:



저작자표시. 귀하는 원 저작자를 표시하여야 합니다.



비영리. 귀하는 이 저작물을 영리 목적으로 이용할 수 없습니다.



변경금지. 귀하는 이 저작물을 개작, 변형 또는 가공할 수 없습니다.

- 귀하는, 이 저작물의 재이용이나 배포의 경우, 이 저작물에 적용된 이용허락조건을 명확하게 나타내어야 합니다.
- 저작권자로부터 별도의 허가를 받으면 이러한 조건들은 적용되지 않습니다.

저작권법에 따른 이용자의 권리와 책임은 위의 내용에 의하여 영향을 받지 않습니다.

이것은 [이용허락규약\(Legal Code\)](#)을 이해하기 쉽게 요약한 것입니다.

[Disclaimer](#)



Ph.D. Dissertation of engineering

Surface modification of layered oxide
cathode materials through phase
segregation for Li ion batteries

상 분리를 통한 리튬이온 전지용
층상계 산화물 양극 소재 표면 개질

2021년 2월

서울대학교 대학원
화학생물공학부

김 한 슬

Ph.D. Dissertation of engineering

Surface modification of layered oxide
cathode materials through phase
segregation for Li ion batteries

상 분리를 통한 리튬이온 전지용
층상계 산화물 양극 소재 표면 개질

2021년 2월

서울대학교 대학원
화학생물공학부

김 한 슬

Surface modification of layered oxide cathode materials through phase segregation for Li ion batteries

Advisor Kyu Tae Lee

Submitting a Ph.D. Dissertation of engineering

February 2021

Graduate School of Engineering
Seoul National University
Chemical and Biological Engineering

Hanseul Kim

Confirming the Ph.D. Dissertation written by

Hanseul Kim

February 2021

Chair	<u>Lee, Won Bo</u>	(Seal)
Vice Chair	<u>Lee, Kyu Tae</u>	(Seal)
Examiner	<u>Choi, Jang Wook</u>	(Seal)
Examiner	<u>Ryu, Ji Heon</u>	(Seal)
Examiner	<u>Mun, Junyoung</u>	(Seal)



Abstract

Interphase engineering is becoming increasingly important in improving the electrochemical performance of cathode materials for rechargeable batteries, including Li-ion, Li metal, and all-solid state batteries, because irreversible surface reactions, such as electrolyte decomposition and transition metal dissolution, constitute one of these batteries' failure modes. In this connection, various coated cathode materials have been investigated to improve interfacial properties. Conventional coating methods using oxides, phosphates and fluorides as coating agents aim the uniformity and the thickness of protective coating layer on an active material. However, a coating layer formed through conventional methods such as dry, wet coating and atomic layer deposition causes an increase in charge transfer resistance by coating planes where Li^+ ions intercalates and deintercalates. This eventually leads to the decrease in rate capability which is critical for high rate demanding applications such as electric vehicles.

Herein, we introduce the out-of-plane-selective epitaxial growth of Li_2SnO_3 on layered oxide cathode materials using the concept of

the thermal phase segregation of Sn-doped $\text{Li}[\text{Ni}_x\text{Co}_y\text{Mn}_z]\text{O}_2$ ($x+y+z=1$) due to the solubility variation of Sn in Sn-doped $\text{Li}[\text{Ni}_x\text{Co}_y\text{Mn}_z]\text{O}_2$ with respect to temperature. For LiCoO_2 , (003) plane-selectively Li_2SnO_3 coated LiCoO_2 is obtained at high temperature (ca. 900°C). Through cross-sectional scanning transmission electron microscopy analyses, it is revealed that the epitaxial growth of Li_2SnO_3 coating layer is due to the large lattice mismatch along the planes perpendicular to the diffusion layer.

Moreover, by investigating the phase segregation behavior in various compositions of layered oxides, essential factors for application of the plane-selective coating method are identified. It is revealed that the presence of Mn^{4+} ions in the host material, structural deterioration is observed at the temperature at which phase segregation occurs. It is also found that plate-like morphology is a crucial factor for epitaxial growth of the Li_2SnO_3 coating layer. By synthesizing Mn-free $\text{Li}[\text{Ni}_{0.80}\text{Co}_{0.15}\text{Al}_{0.05}]\text{O}_2$ cathode materials with plate-like morphology, the (003) plane-selective Li_2SnO_3 coating is achieved for Ni-rich layered oxide cathode material.

Plane-selectively Li_2SnO_3 coated materials exhibit superior rate capability with comparable cycle performance with conventionally coated ones, owing to the absence of Li^+ ion diffusion hindering layer.

This method is promising coating method for layered oxide cathode materials requiring high rate performances.

Keyword : Lithium ion battery, cathode, plane-selective, epitaxial, phase segregation

Student Number : 2016-30230

Table of Contents

1. Introduction	1
2. Backgrounds	4
2.1. Cathode materials for Li ion batteries	4
2.1.1. Co-rich layered oxide	13
2.1.2. Ni-rich layered oxides	15
2.1.3. Surface degradation of layered oxides	18
2.1.4. Conventional surface treatment approaches	22
2.2. Purpose of the research	25
3. Experimental section.....	27
3.1. Synthesis	27
3.1.1. Synthesis of LiCoO ₂ based materials	27
3.1.2. Synthesis of Li[Ni _{0.8} Co _{0.1} Mn _{0.1}]O ₂ based materials	28
3.1.3. Synthesis of Li[Ni _{0.80} Co _{0.15} Al _{0.05}]O ₂ based materials	29

3.1.4. Synthesis of plane selectively Li ₂ SnO ₃ coated Li[Ni _{0.80} Coo _{0.15} Al _{0.05}]O ₂	30
3.1.5. Conventional coating of Li ₂ SnO ₃ on host materials	31
3.2. Material characterization.....	31
3.2.1. Structural analysis	31
3.2.2. TEM analysis.....	33
3.3. Electrochemical characterization	34
3.3.1. Electrode fabrication.....	34
3.3.2. Galvanostatic chargning and discharging	35
3.3.2. AC electrochemical impedance spectroscopy	35
4. Results and discussion	37
4.1. Plane-selective Li₂SnO₃ coating on LiCoO₂	37
4.1.1. Theoretical backgrounds	37
4.1.2. Phase segregation of Li ₂ SnO ₃ on LiCoO ₂	42
4.1.3. Plane selective coating of Li ₂ SnO ₃ on LiCoO ₂	46
4.1.4. Electrochemical performances	55

4.2. Application to Ni-rich layered oxide cathode materials	68
4.2.1. Phase segregation on Li[Ni _{0.8} Co _{0.1} Mn _{0.1}]O ₂	68
4.2.2. Phase segregation on Li[Ni _{0.80} Co _{0.15} Al _{0.05}]O ₂	85
4.2.3. Plane-selective Li ₂ SnO ₃ coating on Li[Ni _{0.80} Co _{0.15} Al _{0.05}]O ₂ through hydrothermal synthesis	91
5. Conclusion	100
References.....	102
국문 초록	111

List of figures

Figure 1. Crystal structures of cathode materials where Li⁺ ions are mobile through 2-dimensional (layered), 3-dimensional (spinel) and 1-dimensional (olivine) frameworks.

Figure 2. Schematic electronic structures of LiFePO₄ and FePO₄.

Figure 3. Schematic mechanism for manganese dissolution from delithiated LiMn₂O₄.

Figure 4. Schematic description of solid–electrolyte interphase destruction mechanism induced by manganese deposition on lithiated graphite.

Figure 5. Structure of distorted layered α -NaFeO₂.

Figure 6. Overall phase changes of Li_{1-x}CoO₂ (1>x>0) during electrochemical delithiation.

Figure 7. (a) schematic electronic structure of redox couples relative to the anion p bands. (b) Crystal structure of partially disordered [Li_{1-x}Ni_x]NiO₂.

Figure 8. The change in amount of dissolved cobalt ion in electrolyte at the various charging voltages.

Figure 9. Schematic degradation mechanism which originated from transition metal dissolution from layered oxide materials.

Figure 10. Theoretical Helmholtz free energy difference between $x\text{Li}_2\text{SnO}_3 + (1-x)\text{LiCoO}_2$ (F_{mix}) and $\text{Li}[\text{Sn}_x\text{Co}_{1-x}]\text{O}_2$ (F_{dop}).

Figure 11. Schematic concept for the synthesis of plane-selectively Li_2SnO_3 coated LiCoO_2 .

Figure 12. XRD patterns of bare LiCoO_2 and 5 at% Sn added LiCoO_2 at various heating temperatures.

Figure 13. Rietveld refinement results of XRD patterns in figure 12.

Figure 14. SEM images of $x\text{Li}_2\text{SnO}_3 + (1-x)\text{LiCoO}_2$, where $x =$ (a) 0, (b) 0.01 (c) 0.02 (d) 0.05.

Figure 15. Cross-sectional STEM-EDS mapping images of Sn 5 at% added LiCoO_2 synthesized at (a) 700 and (b) 900 °C, respectively.

Figure 16. Cross-sectional STEM-EDS line profile of plane-selectively Li_2SnO_3 coated LiCoO_2 .

Figure 17. STEM analysis of plane-selectively Li_2SnO_3 coated LiCoO_2 synthesized with slow cooling rate (1/min). (a) Z-contrast image (b) Enlarged Z-contrast image of red square in (a). FFT pattern of (b) image. (d) Line profile of STEM image intensity across the interface through line 1 along [001] direction in (b).

Figure 18. STEM analysis of plane-selectively Li_2SnO_3 coated LiCoO_2 synthesized with quenching. (a) Z-contrast image (b)

Enlarged Z-contrast image of red square in (a). FFT pattern of (b) image. (d) Line profile of STEM image intensity across the interface through line 2,3 and 4 along [001] direction in (b), respectively.

Figure 19. Powder XRD patterns of bare, plane-selectively Li₂SnO₃ coated and conventionally Li₂SnO₃ coated LiCoO₂.

Figure 20. Cross-sectional STEM-EDS mapping images of the sol-gel derived conventionally Li₂SnO₃ coated LiCoO₂.

Figure 21. Rate performances of conventionally Li₂SnO₃ coated and plane-selectively Li₂SnO₃ coated LiCoO₂.

Figure 22. The voltage profiles of (a) conventionally and (b) plane-selectively Li₂SnO₃ coated LiCoO₂ at various C rates.

Figure 23. Schematic charge-transfer of Li⁺ ions for (a) conventionally Li₂SnO₃ coated LiCoO₂ and (b) plane-selectively Li₂SnO₃ coated LiCoO₂.

Figure 24. Nyquist plots of LiCoO₂/LiCoO₂ symmetric cells for conventionally Li₂SnO₃ coated LiCoO₂ and plane-selectively Li₂SnO₃ coated LiCoO₂.

Figure 25. Cycle performance of conventionally Li₂SnO₃ coated LiCoO₂ and plane-selectively Li₂SnO₃ coated LiCoO₂ at 1C rate.

Figure 26. Cycle performances of bare LiCoO₂ and plane-selectively Li₂SnO₃ coated LiCoO₂ with various Sn compositions.

Figure 27. ICP-MS results of dissolved Co ions in electrolyte after storage at 85°C for 15 days.

Figure 28. The XRD patterns of Sn 2 at% added Li[Ni_{0.8}Co_{0.1}Mn_{0.1}]O₂ synthesized at various temperatures.

Figure 29. The Rietveld refinement results of XRD patterns in figure 28.

Figure 30. Cross-sectional STEM-EDS mapping images of Sn 2 at% added Li[Ni_{0.8}Co_{0.1}Mn_{0.1}]O₂ synthesized at 900°C.

Figure 31. Cycle performances of bare Li[Ni_{0.8}Co_{0.1}Mn_{0.1}]O₂ and Sn 2 at% added Li[Ni_{0.8}Co_{0.1}Mn_{0.1}]O₂ synthesized at various temperatures.

Figure 32. Voltage profiles of formation cycles of bare Li[Ni_{0.8}Co_{0.1}Mn_{0.1}]O₂ and Sn 2 at% added Li[Ni_{0.8}Co_{0.1}Mn_{0.1}]O₂ synthesized at various temperatures.

Figure 33. Two limiting factors that determining the solubility limit of dopants. The relationship between (a) ionic radius of dopants and (b) oxidation state of dopants.

Figure 34. XRD patterns of Sn 2 at% added Li[Ni_{0.8}Co_{0.1+x}Mn_{0.1-x}]O₂ (x=0, 0.05, 0.1) synthesized at 800°C.

Figure 35. Cross-sectional STEM-EDS mapping images of Sn 2 at% added (a) $\text{Li}[\text{Ni}_{0.8}\text{Co}_{0.2}]\text{O}_2$ and (b) $\text{Li}[\text{Ni}_{0.8}\text{Co}_{0.1}\text{Mn}_{0.1}]\text{O}_2$ synthesized at 800°C.

Figure 36. XRD patterns of Sn 5 at% added (a) $\text{Li}[\text{Ni}_{0.80}\text{Co}_{0.15}\text{Al}_{0.05}]\text{O}_2$ and (b) $\text{Li}[\text{Ni}_{0.8}\text{Co}_{0.1}\text{Mn}_{0.1}]\text{O}_2$ synthesized at various temperatures.

Figure 37. The Rietveld refinement results of bare and Sn 5 at% added $\text{Li}[\text{Ni}_{0.80}\text{Co}_{0.15}\text{Al}_{0.05}]\text{O}_2$ and $\text{Li}[\text{Ni}_{0.8}\text{Co}_{0.1}\text{Mn}_{0.1}]\text{O}_2$ at various temperatures.

Figure 38. Cross-sectional STEM-EDS mapping images of Sn 5 at% added $\text{Li}[\text{Ni}_{0.80}\text{Co}_{0.15}\text{Al}_{0.05}]\text{O}_2$ synthesized at 750°C.

Figure 39. Cross-sectional STEM-EDS mapping images of plane-selectively Li_2SnO_3 coated LiCoO_2 at various sites.

Figure 40. Cross-sectional STEM-EDS mapping images 5 at% Li_2SnO_3 segregated on (a) $\text{Li}[\text{Ni}_{0.8}\text{Co}_{0.2}]\text{O}_2$ (b) $\text{Li}[\text{Ni}_{0.8}\text{Co}_{0.1}\text{Mn}_{0.1}]\text{O}_2$ and (c) $\text{Li}[\text{Ni}_{0.80}\text{Co}_{0.15}\text{Al}_{0.05}]\text{O}_2$.

Figure 41. TEM-EDS mapping images of Sn 5 at% added $[\text{Ni}_{0.80}\text{Co}_{0.15}\text{Al}_{0.05}] (\text{OH})_2$ precursors synthesized through hydrothermal method.

Figure 42. The XRD patterns of Sn 5 at% added $\text{Li}[\text{Ni}_{0.80}\text{Co}_{0.15}\text{Al}_{0.05}]\text{O}_2$ synthesized at various temperatures.

Figure 43. The Rietveld refinement results of XRD patterns in figure 42.

Figure 44. Cross-sectional STEM-EDS mapping images of Sn 5 at% added $\text{Li}[\text{Ni}_{0.80}\text{Co}_{0.15}\text{Al}_{0.05}]\text{O}_2$ synthesized at (a) 700°C and (b) 750°C.

Figure 45. Cross-sectional STEM-EDS line profile of plane-selectively Li_2SnO_3 coated $\text{Li}[\text{Ni}_{0.80}\text{Co}_{0.15}\text{Al}_{0.05}]\text{O}_2$.

Figure 46. Rate performances of bare, conventionally and plane-selectively Li_2SnO_3 coated $\text{Li}[\text{Ni}_{0.80}\text{Co}_{0.15}\text{Al}_{0.05}]\text{O}_2$.

1. Introduction

Recent advances in electric vehicles (EVs), which use Li ion batteries as a power source, have shown promise for the expansion of environmentally friendly mobility.¹⁻⁴ However, EVs still require energy storage devices with higher energy density to extend a driving range per charge. In this regards, various materials have been suggested to improve the energy density of Li ion batteries.⁵⁻¹³

The layered oxide cathode materials are widely used for their high structural stability, high operating voltage and high reversible capacity. However, the layered oxide cathode materials suffer from surface related side reactions such as irreversible surface reactions, including electrolyte decomposition and transition metal dissolution, which constitute one of these batteries' failure modes.¹⁴⁻²⁰ In this connection, various coated cathode materials have been investigated to suppress these irreversible surface reactions, leading to improved electrochemical performance.²¹⁻²⁴ Unfortunately, the conventional coating techniques, such as dry coating, sol-gel coating and atomic layer deposition methods,^{21, 25-27} focused only on the uniformity and the thickness of coating layers. These approaches endows the non-

selective coating layers even on the surface where Li^+ ions de-intercalates. Thereby, this makes it hard for us to achieve simultaneous enhancement of rate capability and cycle performance of the cathode material because the coating layer can act as charge transfer resistance by hindering Li^+ ion mobility.

Herein, we introduce a new type of plane-selective coating method on various layered oxide materials using thermal phase segregation of doped materials through the solubility variation of solid solution phases depending on temperatures. For LiCoO_2 , Sn is easily doped in the host structure at low synthesis temperature (*ca.* 700°C), whereas synthesizing at higher temperature (*ca.* 900°C) results in the segregation of Li_2SnO_3 only on the (003) surface of LiCoO_2 due to low solubility limit of Sn at higher temperature. The plane-selectively Li_2SnO_3 coated LiCoO_2 exhibits higher rate and cycle performances than the conventionally coated LiCoO_2 .

Moreover, we also investigated the phase segregation phenomena on Ni-rich $\text{Li}[\text{Ni}_{0.8}\text{Co}_{0.1}\text{Mn}_{0.1}]\text{O}_2$ cathode materials. Through coupled structural and morphological analyses, it was revealed that the presence of Mn^{4+} ions increases the solubility of Sn, and thus the increased synthesis temperature is required for phase segregation of Li_2SnO_3 for $\text{Li}[\text{Ni}_{0.8}\text{Co}_{0.1}\text{Mn}_{0.1}]\text{O}_2$. This leads to the structural

deterioration of the host material in Ni-rich $\text{Li}[\text{Ni}_{0.8}\text{Co}_{0.1}\text{Mn}_{0.1}]\text{O}_2$, eventually results in the degradation of electrochemical performances.

Finally, Mn-free $\text{Li}[\text{Ni}_{0.80}\text{Co}_{0.15}\text{Al}_{0.05}]\text{O}_2$ material was investigated for the plane-selective coating of Li_2SnO_3 on (003) surface of Ni-rich layered oxide cathode material. It was revealed that the morphology of the host material is an important factor for the plane-selective phase segregation on Ni-rich layered oxides as well as the synthesis temperature. Through morphology controlled synthesis via hydrothermal method, we could obtain plane-selectively Li_2SnO_3 coated $\text{Li}[\text{Ni}_{0.80}\text{Co}_{0.15}\text{Al}_{0.05}]\text{O}_2$. The (003) plane-selectively Li_2SnO_3 coated $\text{Li}[\text{Ni}_{0.80}\text{Co}_{0.15}\text{Al}_{0.05}]\text{O}_2$ exhibited higher rate capability than the conventionally coated one. This approach is promising for applications demanding excellent rate performances such as EVs.

2. Backgrounds

2.1. Cathode materials for Li ion batteries

Unlike with conventional primary cells which are designed to be used once, the structural and electrochemical stability of electrode material is one of the most important factor when fabricating rechargeable Li ion batteries. The rechargeable Li ion batteries use electric energy generated from the reduction and oxidation reaction of a certain redox center. Therefore, the redox potential of an electrode material is an important factor that determines the performance of a battery. The redox potential of an electrode material is generally governed by the interaction between redox center (generally, 3d transition metal) and ligands. The bonding character of the redox center and ligands is dependent on the distance and strength of the bonding, which is closely related with the structure of a material. In this connection, various cathode materials have been explored which have variety structures. Cathode materials are generally classified into 3 types according to the channels through which Li^+ ions diffuse within the material, as shown in **figure 1**.

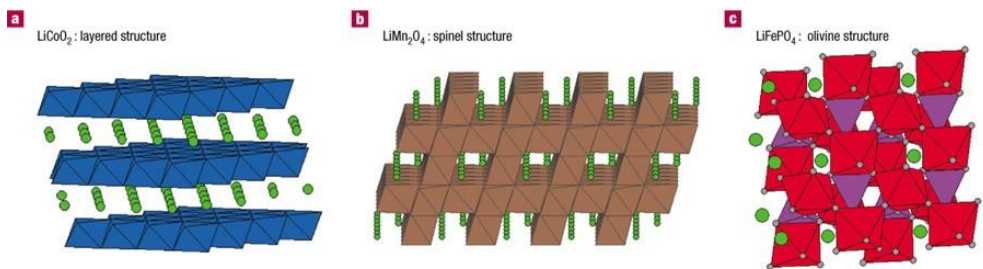


Figure 1. Crystal structures of cathode materials where Li^+ ions are mobile through 2-dimensional (layered), 3-dimensional (spinel) and 1-dimensional (olivine) frameworks.⁵

Olivine structure which is represented by LiFePO₄ is a material that has 1-dimensional diffusion channel. Olivine LiFePO₄ exhibits high safety which is critical for battery operation.²⁸ The high safety of LiFePO₄ is attributed to the inductive effect of PO₄ tetrahedron.^{29, 30} The inductive effect which stems from strong bonding character of P–O bond reduces covalent character of Fe–O bond, which inhibits overlapping of Fe 3d and O 2p band.^{31, 32} It has been reported that the overlapping of transition metal and O state is closely related with the safety of the material in that it causes O₂ gas evolution from the host material.^{33, 34} (**Figure 2**) Despite the advantages of high safety and stable cycle performance, the olivine LiFePO₄ is not considered as the best option for batteries demanding high power density due to its low electronic conductivity which stems from the localized electrons in strong P–O bond. Therefore, the use of LiFePO₄ is limited to small electric devices such as power tools.

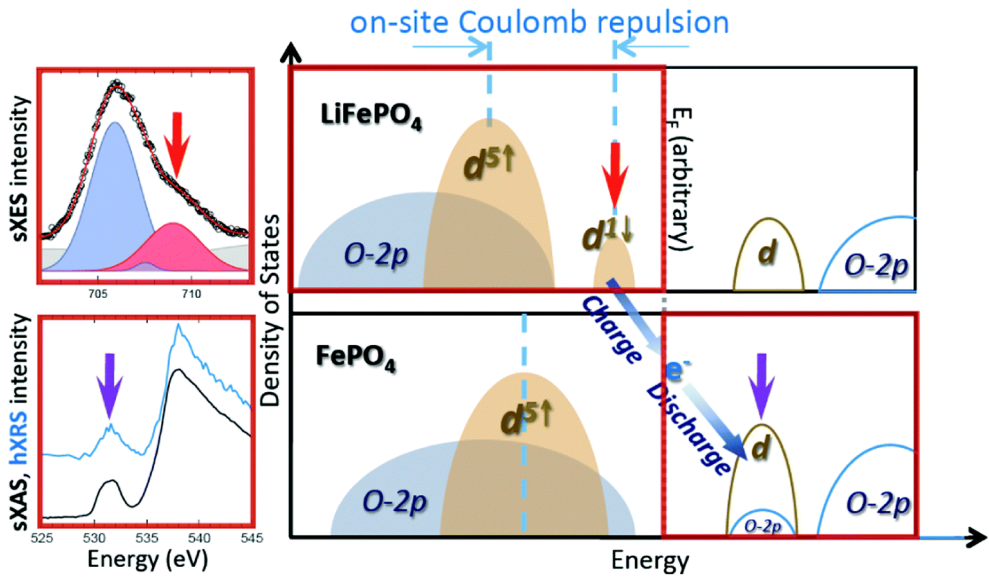


Figure 2. Schematic electronic structures of LiFePO_4 and FePO_4 .³⁵

Spinel LiMn₂O₄ is a material that has 3-dimensional Li⁺ ion diffusion channel with superior rate capability.^{36, 37} Moreover, LiMn₂O₄ can be synthesized via solid-state reaction which is feasible for mass production. The low cost of Mn source and environmental amity also make spinel LiMn₂O₄ as a promising cathode material for Li ion batteries. However, spinel LiMn₂O₄ cathode material suffers serious capacity fading stems from dissolution of Mn²⁺ cations into the electrolyte by HF corrosion.^{38, 39} (**Figure 3**) The dissolved Mn²⁺ ions in electrolyte migrates to anode surface and induce self-discharge of lithiated graphite. On the surface of lithiated graphite (LiC₆), the electrode potential is low enough (~0.0 V) to Mn²⁺ ion to be reduced to Mn⁰. Simultaneously, Li⁺ ions are extracted from lithiated graphite to bulk electrolyte, which is called self-discharge, as shown in **figure 4.**^{40, 41} The deposited Mn metal on graphite increases the rate of electrolyte decomposition, especially for ethylene carbonate, which finally results in internal cell failure.

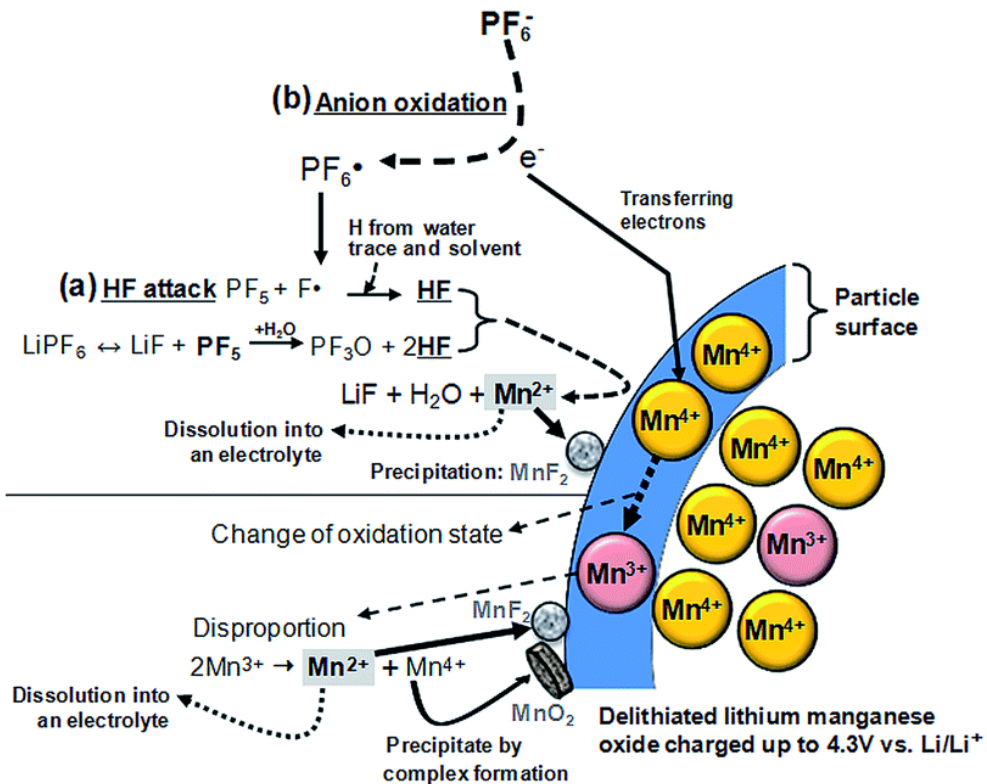


Figure 3. Schematic mechanism for manganese dissolution from delithiated LiMn_2O_4 .⁴²

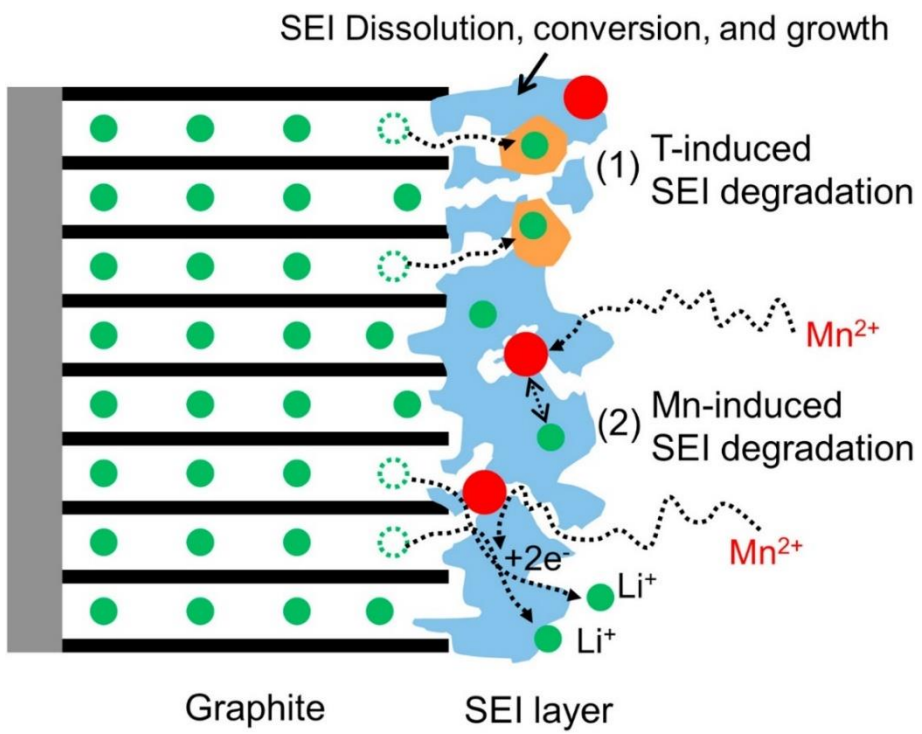


Figure 4. Schematic description of solid–electrolyte interphase destruction mechanism induced by manganese deposition on lithiated graphite.⁴⁰

Layered oxide cathode material is the most widely used cathode material for current Li ion battery system. Layered oxide cathode material has chemical formula of LiTMO_2 where TM is 3d transition metal ions such as Ni, Co, Mn and their combination.^{11, 43} In LiTMO_2 structure, which is an analogues to $\alpha-\text{NaFeO}_2$ structure, O^{2-} ions are stacked in close-cubic packing (CCP), which act as framework of the structure. Within the CCP of O^{2-} ions, Li^+ ions and TM^{3+} ions occupy octahedral sites with altering layers in [111] direction, as shown in **figure 5**. Therefore, layered oxide cathode material has 2-dimensional Li^+ ion diffusion channel between oxygen slabs, which allows layered oxide cathode materials to deliver excellent rate capability. In general, along with the fast Li^+ ion kinetics, layered oxide cathode materials are synthesized via solid-state reaction, which give feasibility to mass production. Moreover, the large window for elements resides in transition metal ion sites provides a variety of structure for their application.

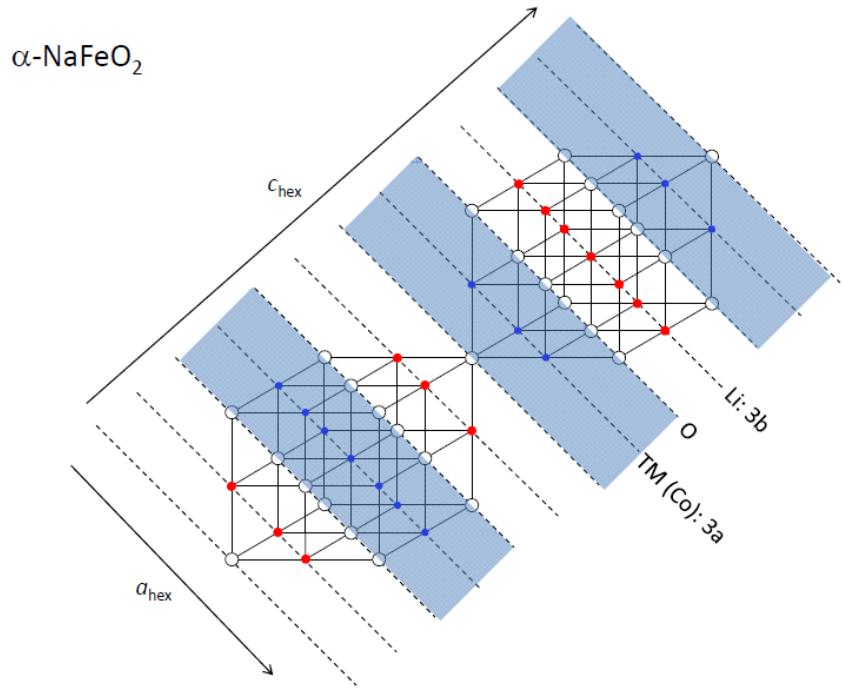


Figure 5. Structure of distorted layered $\alpha\text{-NaFeO}_2$.

2.1.1. Co-rich layered oxides

Among the layered oxide cathode materials, LiCoO_2 is the most widely used cathode materials for Li ion battery system.⁴⁴ Large difference in ionic radius of Li^+ ions and Co^{3+} ion gives completely separated layers within O^{2-} slabs, which enables high rate capability. During charge and discharge, a redox reaction between $\text{Co}^{3+/4+}$ occurs with intercalation and deintercalation of Li^+ ions.

The LiCoO_2 undergoes various phase transition during delithiation, as shown in **figure 6**.^{45–48} When Li^+ ions are extracted from $\text{Li}_{1-x}\text{CoO}_2$ ($x < 0.5$), the Li slab expands due to the electrostatic repulsion between O^{2-} slabs, which facilitates Li^+ ion mobility. When 50% of Li^+ is extracted, *ca.* $\text{Li}_{0.5}\text{CoO}_2$ composition, LiCoO_2 undergoes phase transition from hexagonal to monoclinic which is called “order-disorder transition”. When more Li^+ ions are extracted over 90%, the transformation of oxygen stacking sequence from O3 (ABCABC stacking sequence) to O1 (ABAB stacking sequence) occurs, which accompanied with the Fermi level shifting into the valence band. Consequently, $\text{Co}^{3+/4+}$ t_{2g} and O^{2-} 2p band are hybridized, which leads to oxidation of O^{2-} ions. The oxidation of O^{2-} ions results in the evolution of O_2 gas evolution, which causes irreversible phase

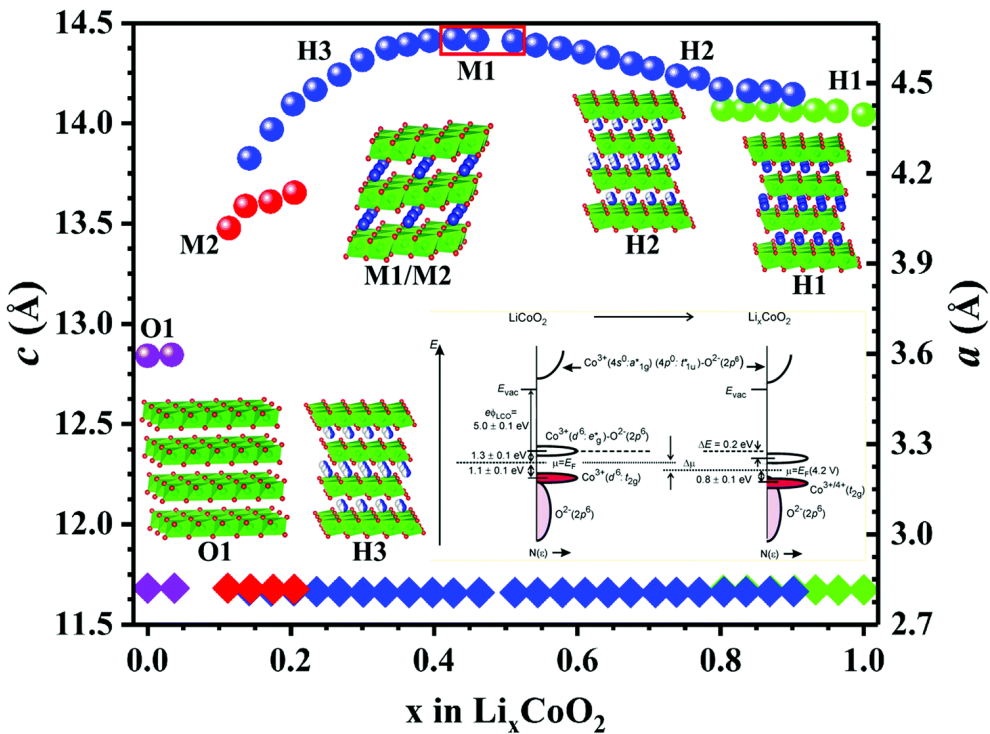


Figure 6. Overall phase changes of $\text{Li}_{1-x}\text{CoO}_2$ during electrochemical delithiation.⁴⁸

transition and reduce cell safety during cycling.^{49, 50}

Moreover, it is known that instability of surface structure at high operating voltage causes irreversible electrolyte decomposition and Co dissolution in conventional LiPF₆ based electrolytes.^{45, 51} The detailed surface degradation mechanism will be dealt in later section. To sum up, although the LiCoO₂ shows excellent electrochemical performances, the utilization of Li⁺ ions from LiCoO₂ is limited to nearly ~50% with operating voltage below 4.2 V.

2.1.2. Ni-rich layered oxides

The limited utilization of LiCoO₂ act as a great hurdle for large scale energy storage systems and electric vehicles, which demands high volumetric and gravimetric energy density. Moreover, instability of market price of cobalt precursor such as cobalt carbonate requires new type of layered cathode material. In this connection, Ni-rich layered oxide is one of the most promising alternatives to Co-rich layered oxide cathode material. Ni-rich layered oxide materials can deliver high reversible capacity (> 200 mAh g⁻¹) compared to Co-rich oxide materials.

The origin of high reversible capacity of Ni-rich layered oxide is known to stem from its electronic structure. As mentioned earlier, the overlapping of $\text{Co}^{3+/4+}$ t_{2g} band of oxidized LiCoO_2 overlaps with O^{2-} 2p band to induce irreversible oxidation of O^{2-} from the host structure. However, it is known that the overlapping of $\text{Ni}^{3+/4+}$ eg and O^{2-} 2p band is less than that of $\text{Co}^{3+/4+}$ t_{2g} and O^{2-} 2p, as shown in **figure 7**. Therefore, the oxidation of O^{2-} is mitigated in Ni-rich layered oxides to deliver higher reversible capacity than Co-rich layered oxides.⁵⁰

However, it is difficult to synthesize stoichiometric composition due to inevitable site exchange between $\text{Li}^+/\text{Ni}^{2+}$ cation disorder. It is known that Ni ion has tendency to be formed as Ni^{2+} , which has similar ionic size with Li^+ . Owing to this similarity in ionic radii, Ni^{2+} ions tend to occupy octahedral sites in Li-layer, which is called cation disorder.⁵²⁻⁵⁵ Li^+ ion diffusion is hindered in this partially disordered Li layer in that the Ni^{2+} ions in Li-layer act as blocking pillar during de-/lithiation process, giving poor rate capability of the material.

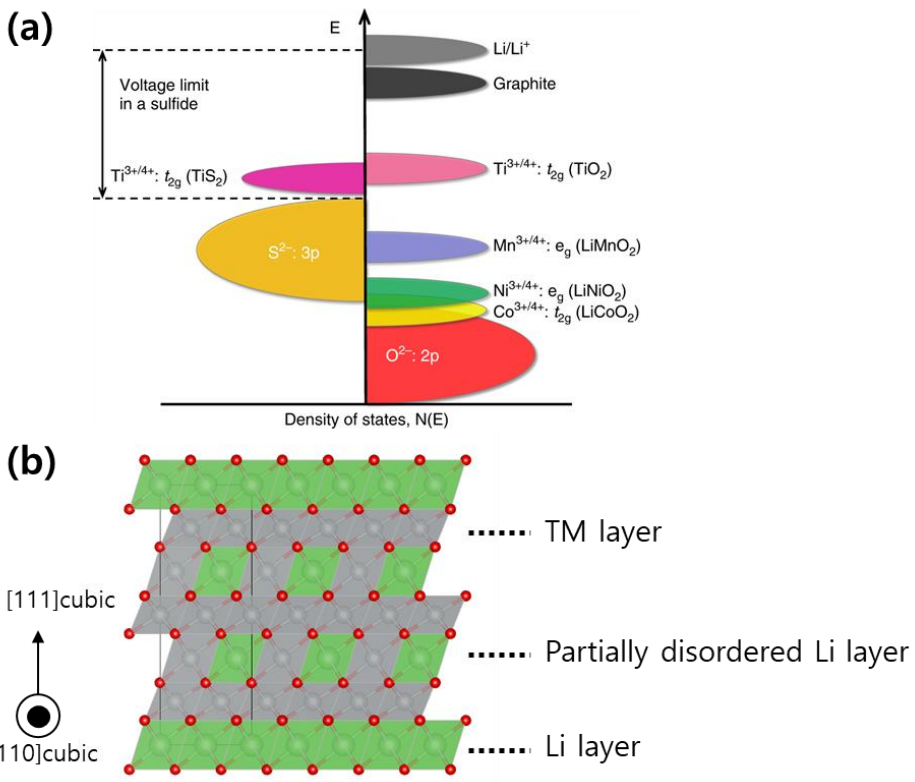


Figure 7. (a) Schematic electronic structure of redox couple relative to the anion p bands.⁵⁶ (b) Crystal structure of partially disordered $[Li_{1-x}Ni_x]NiO_2$.

2.1.3. Surface degradation of layered oxide cathode materials

Although Co-rich and Ni-rich layered oxide cathode materials have their strength in rate capability and high reversible capacity, respectively, they both suffer from surface-related side reactions. These side reactions including transition metal dissolution, salt and solvent decomposition and crack formation are not fully understood due to their complexity.

Conventionally known degradation mechanism of layered cathode material proposed in 1996 is transition metal dissolution from host material.⁵¹ As shown in the figure 8, the oxidized $\text{Li}_{1-x}\text{CoO}_2$ undergoes severe Co dissolution from host material over 4.4 V (vs. Li/Li^+). Later, it is reported that Ni-rich layered oxide cathode materials also suffer from the similar degradation phenomenon.^{57, 58} The origin of transition metal dissolution is known to be the corrosion by hydrofluoric acid (HF) generated via decomposition of LiPF_6 and other fluorine-containing species. LiPF_6 , the most widely used salt for Li-ion battery system, shows good chemical and thermal stability under dry and inert atmosphere. However, when LiPF_6 is exposed to traces of H_2O , the salt decomposes to form HF following reaction below;

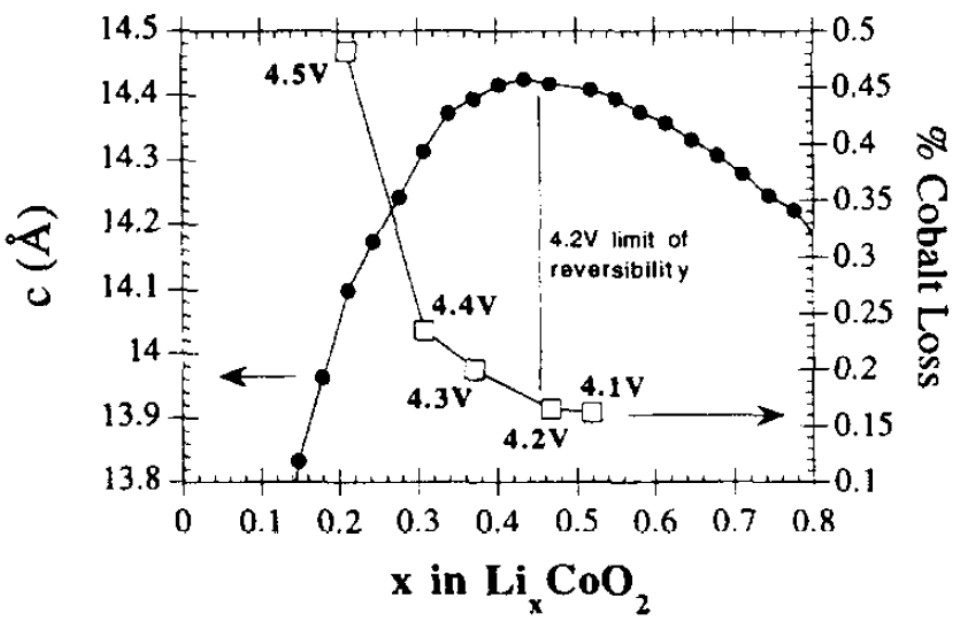
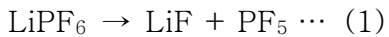


Figure 8. The change in amount of dissolved cobalt ion in electrolyte at the various charging voltages.⁵¹



The formation reaction of HF can be catalyzed by the presence of alcohols that can be a product of decomposition of carbonate solvents at high voltage such as ethylene carbonate (EC).^{38, 59} The dissolution of transition metal ion from the surface of host material results in the phase transition from layered to spinel or rock-salt phase, which is known to increase charge transfer reaction at the surface.^{60, 61} Recently, the dissolution of Mn²⁺ ions from Ni-rich oxides and their deposition on anode surface leads to severe capacity degradation during cycling.⁵⁸ The dissolved Mn²⁺ ions are reduced to Mn⁰ metal on the surface of anode, simultaneously extracting Li⁺ ions from lithiated graphite, which is called “self-discharge”. This irreversible self-discharge from anode results in the decrease in charge carrier, which is especially critical to full cell.

Electrolyte decomposition is also one of the most critical problems of surface originated degradation. In conventional system, the electrolyte is composed of salt that contains charge carrier such as LiPF₆, LiFSI or LiClO₄ and organic liquid solvents that can dissolve salts.^{62, 63} Among solvents, cyclic carbonates such as ethylene

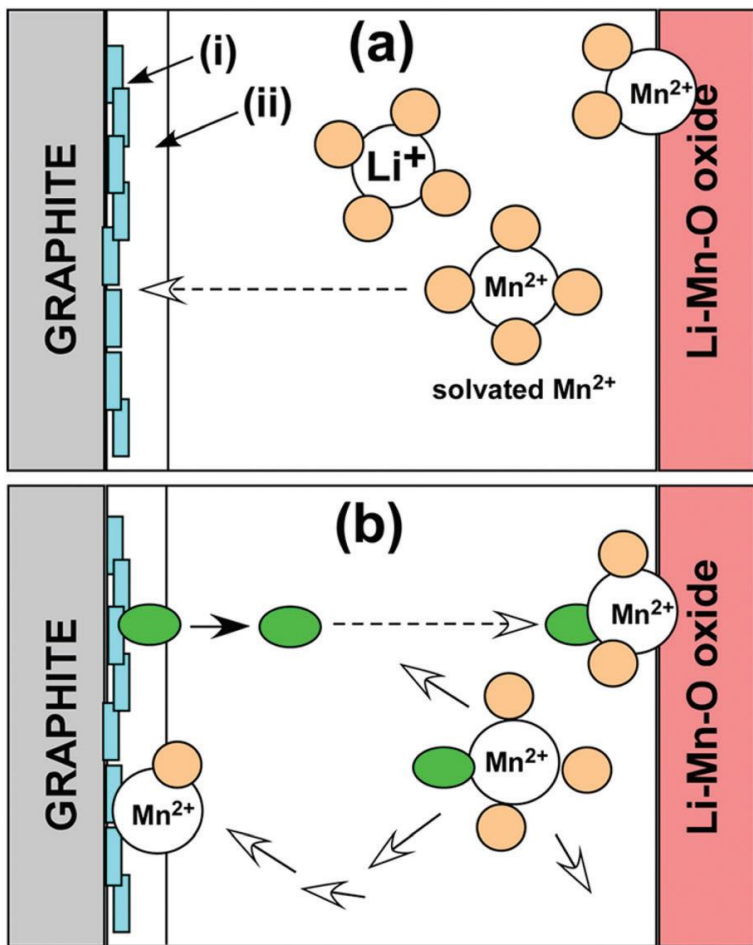


Figure 9. Schematic degradation mechanism which originated from transition metal dissolution from layered oxide materials.⁶⁴

carbonate (EC) and propylene carbonate (PC) are used due to high dielectric property, which has high solvation strength. Along with high dielectric property, the viscosity of solvent increases due to increase in polarity. Therefore, the mixture of solvents with high dielectric property and low viscosity is used for electrolyte.

Among cyclic carbonates, only EC can be used for Li ion batteries in that PC is known to induce graphite exfoliation generated from the co-intercalation of Li^+ solvated complexes. Unfortunately, EC is known to be decomposed on the surface of cathode with high voltage to produce gaseous byproducts such as CO or CO_2 .^{65, 66} This irreversible gas evolution reaction results in low coulombic efficiency as well as degradation of cell performance and safety. Therefore, the enhancing surface stability of layered oxide cathode material is increasingly important.

2.1.4. Conventional surface treatment approaches

With increasing need for materials with high surface stability, many surface treatment methods were explored. Forming coating layer on the surface of cathode material is one of the most powerful method

of increasing surface stability of cathode materials. Coating layer protects a physically or chemically to suppress the contact between active material and external substances such as electrolyte, H₂O, HF and CO₂.

Coating layer is usually an electrical insulator to inhibit tunneling of electron from active materials to external substances. In this connection, various coating materials were suggested including oxides (Al₂O₃, ZrO₂, TiO₂, MgO, ZnO, etc.), phosphates (Li₃PO₄, AlPO₄, Mn₃(PO₄)₂, etc.), fluorides (AlF₃, MgF₂, etc.) and sulfides (MoS₂, TiS₂, etc.).^{21, 22, 67-78} For example, various metal oxides such as Al₂O₃, TiO₂ and ZrO₂ coated on layered oxide are known to effectively reduces Co dissolution from LiCoO₂, which enables use in higher operating voltage range.⁷⁹ Moreover, when thermally stable material is coated on the surface of an active material, it is reported that the thermal stability is enhanced.^{73, 80, 81} This improvement is owing to the reduced active surface area between an active material and electrolyte.

To achieve surface coating layer, several methods were developed such as dry coating, wet coating and atomic layer deposition (ALD). Dry coating method involves the mechanical mixing the cathode powder with the coating precursor powder.^{22, 25} This method has

advantage in mass production in aspect of highly simple and safe procedure. For instance, nanosized SiO_2 particle was coated on $\text{Li}[\text{Ni}_{0.80}\text{Co}_{0.15}\text{Al}_{0.05}]\text{O}_2$ (NCA) active material to enhance thermal stability. With the amphoteric character of SiO_2 coating layer, NCA particle is protected from surface byproducts such as acidic species and electrolyte.⁸² Unfortunately, it is known that the surface coating layer synthesized via dry coating method is locally distributed on active material. Therefore, achieving uniform thickness of coating layer is quite difficult, which results in lack of reproducibility of electrochemical performance.

Another method of forming a protective layer on the surface of an active material is a solution-based wet coating method.⁷⁹ This method allows relatively uniform coating layer in comparison to the dry coating method. In detail experimental process, both active material and coating precursors are dispersed in volatile solvents, followed by evaporation of solution and post-heat treatment. This method has the advantage of being able to form various coatings from phosphates to fluorides and oxides as a coating layer while providing moderate coverage. However, safety issue arises from the usage of volatile character of the solvents used in this process.

Atomic-layer deposition is a method that provides homogeneous

coating layer to active material.^{68, 83, 84} This approach is a gas–phase method of thin–film growth using sequential, self–limiting surface reactions. Moreover, this reaction requires minimal amount of precursors in contrary to sol–gel based wet coating method. For instance, several Ångstrom(Å)–thick Al₂O₃ was coated on LiCoO₂ via ALD method showed remarkable improvement of electrochemical properties. Although ALD yields good coverage and superior electrochemical improvements, it is not an adequate coating method for commercialization due to difficulty of mass production and cost ineffectiveness.

2.2. Purpose of the research

Although the conventional coating methods mentioned above have extended the limits of application of layered oxide cathode materials for Li ion batteries, some problems are still being raised such as production cost and safety issues arise from additional process and use of volatile solvents, respectively. Moreover, recent studies show that surface of primary particle also undergoes degradation during extensive cycling. The conventional coating methods provides

coating layers on secondary particles because the coating process is conducted after the synthesis of an active material. In this case, the electrolyte can penetrate into inner primary particles once small defect of the coating layer on the secondary particle is created. The penetration of electrolyte into uncoated primary particle can cause consecutive degradation of an active material during extensive cycling. Therefore, it is essential to find new type of surface treatment method for layered oxide cathode materials.

Adopting phase segregation can be a promising method for a new type of surface treatment. The elements can be doped in layered oxide cathode materials have different solubility limit with respect to temperature. When concentration of dopants is beyond their solubility limit, dopants tend to diffused out to free surfaces. Surface segregation from a grain provides primary particles with conformal coating layer within the secondary particles, which can also act as glue that prevents primary particles from apart each other. Moreover, it also reduces production costs in that it does not need additional process which is required in the conventional coating method.

3. Experimental section

3.1. Synthesis

3.1.1. Synthesis of LiCoO₂ based materials

Bare LiCoO₂, Sn-doped LiCoO₂, and plane-selectively Li₂SnO₃ coated LiCoO₂ powders were synthesized using a simple sol-gel method. LiNO₃ (Sigma Aldrich), Co(NO₃)₂·6H₂O (Sigma Aldrich) and SnCl₂ (Alfa Aesar) precursors were dissolved in ethanol. The molar ratios of precursors were Li : Co : Sn = 1.03(1+x) : 1-x : x where x = 0, 0.01, 0.02, and 0.05. Citric acid (Sigma Aldrich) as a chelating agent was added as much as the total molar amount of all cations. The solutions were stirred for 6 hours at 80°C to obtain transparent gels, followed by being dried in a vacuum oven overnight to exterminate solvents. Homogenously mixed powders were heated in air at 300°C for 5 hours. Then they were reheated in air for 10 hours at 700°C to obtain and Sn-doped LiCoO₂, and at 900°C to obtain bare LiCoO₂ and plane-selectively Li₂SnO₃ coated LiCoO₂ powders. The heating rate was 10°C min⁻¹ for all samples and the cooling rate was about 1°C

min^{-1} for plane-selectively Li_2SnO_3 coated LiCoO_2 powders.

3.1.2. Synthesis of $\text{Li}[\text{Ni}_{0.8}\text{Co}_{0.1}\text{Mn}_{0.1}]\text{O}_2$ based materials

Bare $\text{Li}[\text{Ni}_{0.8}\text{Co}_{0.1}\text{Mn}_{0.1}]\text{O}_2$, Sn-doped $\text{Li}[\text{Ni}_{0.8}\text{Co}_{0.1}\text{Mn}_{0.1}]\text{O}_2$ and Li_2SnO_3 coated $\text{Li}[\text{Ni}_{0.8}\text{Co}_{0.1}\text{Mn}_{0.1}]\text{O}_2$ were synthesized using a simple sol-gel method. LiNO_3 (Sigma Aldrich), $\text{Ni}(\text{NO}_3)_2 \cdot 6\text{H}_2\text{O}$, $\text{Co}(\text{NO}_3)_2 \cdot 6\text{H}_2\text{O}$ (Sigma Aldrich), $\text{Mn}(\text{NO}_3)_2 \cdot 4\text{H}_2\text{O}$ and SnCl_2 (Alfa Aesar) precursors were dissolved in ethanol. The molar ratios of precursors were $\text{Li: Ni: Co: Mn: Sn} = 1.03(1+x): 0.8(1-x): 0.1(1-x): 0.1(1-x): x$ where $x = 0, 0.01, 0.02,$ and 0.05 . All procedures before second heat treatment followed the same procedure in 3.1.1. After heating at 300°C for 5 hours, powders were reheated in flow of O_2 for 10 hours at 800°C to obtain bare $\text{Li}[\text{Ni}_{0.8}\text{Co}_{0.1}\text{Mn}_{0.1}]\text{O}_2$. To obtain Sn-doped $\text{Li}[\text{Ni}_{0.8}\text{Co}_{0.1}\text{Mn}_{0.1}]\text{O}_2$, powders were heated at 860 and 880°C for 10 hours with O_2 flow. For phase segregated mixture of Li_2SnO_3 and $\text{Li}[\text{Ni}_{0.8}\text{Co}_{0.1}\text{Mn}_{0.1}]\text{O}_2$, powders were heated at 900 for 10 hours with O_2 flow. The heating rate was $10^\circ\text{C min}^{-1}$ for all samples and the cooling rate was about 1°C min^{-1} .

3.1.3. Synthesis of Li[Ni_{0.80}Co_{0.15}Al_{0.05}]O₂ based materials

Bare Li[Ni_{0.80}Co_{0.15}Al_{0.05}]O₂, Sn-doped Li[Ni_{0.80}Co_{0.15}Al_{0.05}]O₂ and Li₂SnO₃ coated Li[Ni_{0.80}Co_{0.15}Al_{0.05}]O₂ were synthesized using a simple sol-gel method. LiNO₃ (Sigma Aldrich), Ni(NO₃)₂·6H₂O, Co(NO₃)₂·6H₂O (Sigma Aldrich), Al(NO₃)₂·9H₂O and SnCl₂ (Alfa Aesar) precursors were dissolved in ethanol. The molar ratios of precursors were Li: Ni: Co: Al: Sn = 1.03(1+x): 0.8(1-x): 0.15(1-x): 0.05(1-x): x where x = 0 and 0.05. All procedures before second heat treatment followed the same procedure in 3.1.1.

After heating at 300°C for 5 hours, powders were reheated in flow of O₂ for 10 hours at 750°C to obtain bare Li[Ni_{0.80}Co_{0.15}Al_{0.05}]O₂. To obtain Sn-doped Li[Ni_{0.80}Co_{0.15}Al_{0.05}]O₂, powders were heated at 700°C for 10 hours with O₂ flow. For phase segregated mixture of Li₂SnO₃ and Li[Ni_{0.80}Co_{0.15}Al_{0.05}]O₂, powders were heated at 750 for 10 hours with O₂ flow. The heating rate was 10°C min⁻¹ for all samples and the cooling rate was about 1°C min⁻¹.

3.1.4. Synthesis of plane-selectively Li₂SnO₃ coated Li[Ni_{0.80}Co_{0.15}Al_{0.05}]O₂

The [Ni_{0.80}Co_{0.15}Al_{0.05}]_{0.95}Sn_{0.05}(OH)₂ precursors were synthesized through hydrothermal method. Ni(NO₃)₂·6H₂O, Co(NO₃)₂·6H₂O (Sigma Aldrich), Al(NO₃)₂·9H₂O SnCl₂ (Alfa Aesar) precursors were dissolved in 30 mL of ethanol. The molar ratios of precursors were Li: Ni: Co: Al: Sn = 1.03(1+x): 0.8(1-x): 0.15(1-x): 0.05(1-x): x where x = 0 and 0.05. Then, 0.3 g of Polyvinylpyrrolidone (PVP, average molar mass = 29000) was dissolved in the solution as a surfactant. The solution was sealed in 100 mL Teflon-lined autoclave and heated at 180°C for 10 hours. The precipitates were washed for 4 times with water and ethanol, respectively, and separated with solution by centrifuging. The powders were dried in vacuum oven at 80°C for overnight to exterminate trace of water.

Plane-selectively Li₂SnO₃ coated Li[Ni_{0.80}Co_{0.15}Al_{0.05}]O₂ were synthesized through solid-state reaction between LiOH•H₂O and the synthesized [Ni_{0.80}Co_{0.15}Al_{0.05}]_{0.95}Sn_{0.05}(OH)₂ precursor. The molar ratio of precursors were 1.08: 1. The mixed powders were heated at 750°C for 10 hours under O₂ flow. The heating rate was 10°C min⁻¹ for all samples and the cooling rate was about 1°C min⁻¹.

3.1.5. Conventional coating of Li₂SnO₃ on host materials

Conventional sol-gel derived Li₂SnO₃ coated LiCoO₂ and Li[Ni_{0.80}Co_{0.15}Al_{0.05}]O₂ were obtained according to the previously reported method. LiNO₃ (Sigma Aldrich) and Tin(IV) ethylhexanoisopropoxide (Alfa Aesar) were dissolved in 2-Propanol (Alfa Aesar) with the molar ratio of Li : Sn = 2 : 1. Bare LiCoO₂ and Li[Ni_{0.80}Co_{0.15}Al_{0.05}]O₂ powders were dispersed in the solution with the molar ratio of Li₂SnO₃: LiCoO₂ (or Li[Ni_{0.80}Co_{0.15}Al_{0.05}]O₂) = 0.05: 0.95. The mixtures were dried using a rotary evaporator at 50 °C to remove solvents. Then, powders were heated in air at 750 and 800 °C for 6 hours for Li[Ni_{0.80}Co_{0.15}Al_{0.05}]O₂ and LiCoO₂, respectively.

3.2. Material characterization

3.2.1. Structural analysis

X-ray Diffraction (XRD) analysis is a powerful tool when determining the atomic structure of a crystal. When X-ray beam is radiated in a crystal with a periodic atomic arrays, the constructive

interference between scattered radiation occurs to a specific angle (Bragg's angle). This bragg approach is to regard crystals as built up in layers or planes such that each acts as a semi-transparent mirror. Therefore, the distance between planes can be calculated with bragg's law ($\lambda = 2d \sin \theta$), where λ is X-ray wavelength and d is distance between the mirror-like adjacent planes.

From the XRD profiles, interpretation of crystallographic information such as unit cell parameters, atomic parameters, crystallinity, disorder and defects is possible through the Rietveld refinement method. The Rietveld refinement method is a way of fitting technique that fits a calculated profile to an experimental data by employing non-linear least square method. The unit cell parameter information such as a, b, c, α , β , γ , etc. is obtained with the peak positions of the profile. The atomic parameters including atom positions and thermal factor are dependent on the peak intensities. Moreover, the macroscopic information such as crystallinity, strain and stress is represented by the peak shapes of the profiles. Therefore, combining XRD and the Rietveld refinement method is essential for understanding the structural information of the crystals.

XRD patterns of powders and electrodes were obtained using a

Bruker D2 PHASER with Cu K α radiation ($\lambda = 1.5418 \text{ \AA}$) operated in the 2θ range of 10–80°. The lattice parameters and the occupancies of atoms were obtained from full pattern matching refinements using the TOPAS program.

3.2.2. TEM analysis

Transmission electron microscopy (TEM) is a microscopy technique that provides atomic scale resolution by using electron beam. The images are formed from the interaction of the electrons with the sample as the electron beam is transmitted through the sample. Generally, due to the short wavelength of electron wave (*ca.* 2.73 pm, at 200 keV accelerated beam), the resolution of a TEM is high enough to observe atomic arrays of the sample (*ca.* 0.2 nm).

In this study, a scanning transmission electron microscope (STEM) is used rather than high resolution TEM (HR-TEM) because STEM yields higher resolution in atomic scale. In STEM, two types of images can be obtained such as high-angle annular dark-field (HAADF) and bright field (BF) images with respect to the detectors. Particularly, by using HAADF detector, it is possible to obtain atomic

resolution images where the contrast of an atoms is directly related to the atomic number. Moreover, energy-dispersive X-ray spectroscopy (EDS) information can be obtained, which provides compositional information and elemental mapping images of the samples.

TEM samples were examined using a high-resolution transmission electron microscope (HR-TEM, STEM, JEOL ARM-200F). Cross-sectional thin STEM specimens were obtained using the Ar ion slicer (JEOL EM-09100 IS). FE-SEM images were obtained using an FE-SEM (JSM-6701F, JEOL Ltd).

3.3. Electrochemical characterization

3.3.1. Electrode fabrication

To investigate electrochemical properties, thin film cathode was fabricated by mixing active material, conducting carbon and binder. Active materials were mixed with carbon black (Super P, TIMCAL) and polyvinylidene fluoride (PVdF, KF-1100, Kureha) in a weight ratio of 8:1:1. The slurry was cast onto a 20 μm thick current collector

(Al foil). The electrodes were dried at 120°C overnight in a vacuum oven to exterminate trace of water. The mass loading of active materials in electrodes is 5.5 – 6 mg cm⁻². The thickness of the cathode laminate is ~20 μm.

3.3.2. Galvanostatic charging and discharging

The electrochemical performance of half cells was evaluated using 2032 coin cells with a Li metal (Honjo metal Co. Ltd.) and 1.3 M LiPF₆ in ethylene carbonate, ethylmethyl carbonate and dimethyl carbonate (30:40:30 vol.%, Soulbrain Co. Ltd.). Galvanostatic experiments of the electrodes were performed using WBCS 3000 (WonATech, Korea) at 25°C. The current densities and operating voltage windows were varied with respect to the active materials. For LiCoO₂, cycle tests were performed at a current density of 1 C rate (160 mA g⁻¹) after precycling at 0.1 C rate (16 mA g⁻¹) within the voltage ranges between 3.0–4.5 V (vs. Li/Li⁺). For Ni-rich Li[Ni_{0.8}Co_{0.1}Mn_{0.1}]O₂ and Li[Ni_{0.80}Co_{0.15}Al_{0.05}]O₂, cycle tests were performed at a current density of 0.5 C rate (100 mA g⁻¹) after precycling at 0.1 C rate (20 mA g⁻¹) within the voltage ranges between 3.0–4.4 V (vs. Li/Li⁺).

3.3.3. AC electrochemical impedance spectroscopy

Electrochemical impedance spectroscopy (EIS) was measured using LiCoO₂/LiCoO₂ symmetric cells with an amplitude of 5 mV over a frequency range of 0.005 to 100 kHz. The electrodes used for LiCoO₂/LiCoO₂ symmetric cells were charged upto 4.05 V (vs. Li/Li⁺) after 1st precycle.

4. Results and Discussion

4.1. Plane-selective Li₂SnO₃ coating on LiCoO₂

4.1.1. Theoretical backgrounds

Theoretical background of phase segregation of Li₂SnO₃ and LiCoO₂ was investigated through density functional theory (DFT) calculation.

Among various thermodynamic variables, the Helmholtz energy was calculated to compare phase stability of LiCoO₂, Li₂SnO₃, and Sn-doped LiCoO₂. Comparing the Helmholtz energy is reasonable when considering the thermodynamic stability of phase stability of solids.

The Helmholtz free energy is defined as following equations 3.

$$A = U - TS \cdots (3)$$

A is the Helmholtz free energy, U is the internal energy, T is temperature and S is the entropy. Considering that temperature and volume is a natural pair of variables, differentiated expression for A can be denoted as equation 4.

$$dA = dU - Tds - SdT \dots (4)$$

Using the combined mathematical form of first and second laws of thermodynamics, the differentiated expression can also be denoted as equation 5.

$$dA = -pdV - SdT \dots (5)$$

Thus, the Helmholtz free energy represents the thermodynamic potential at constant volume. Considering that the volume expansion of unit cell with respect to the temperature is negligible in solids, the Helmholtz free energy shows temperature dependent behavior. In this condition, the lower the Helmholtz free energy, the more thermodynamically stable phase.

Figure 10 shows the difference between the Helmholtz free energies ($F_{mix} - F_{dop}$) of $x\text{Li}_2\text{SnO}_3 + (1-x)\text{LiCoO}_2$ (F_{mix}) and $\text{Li}[\text{Sn}_x\text{Co}_{1-x}]\text{O}_2$ (F_{dop}). X is assumed to be 0.08 in the calculation, because this value corresponds to the ratio of one Sn atom in the super cell of LiCoO_2 used in the calculation. The value of $F_{mix} - F_{dop}$ is positive at temperatures below *ca.* 1000 K, implying that Sn-doped LiCoO_2 is

thermodynamically more stable than the mixture of $x\text{Li}_2\text{SnO}_3$ and $(1-x)\text{LiCoO}_2$ at these temperatures.). The value of $F_{mix} - F_{dop}$, however, decreases with increasing temperatures. Eventually, this value turns positive to negative at *ca.* 1000 K. This indicates that the mixture of $x\text{Li}_2\text{SnO}_3$ and $(1-x)\text{LiCoO}_2$ is more stable than Sn-doped LiCoO_2 at $> ca.$ 1000 K.

The DFT calculation result demonstrates that heat treatment over 1000K results in the phase segregation of Li_2SnO_3 and LiCoO_2 , which shows the possibility of one-step surface coating using the thermal dependence of solubility of Sn, following scheme in **figure11**.

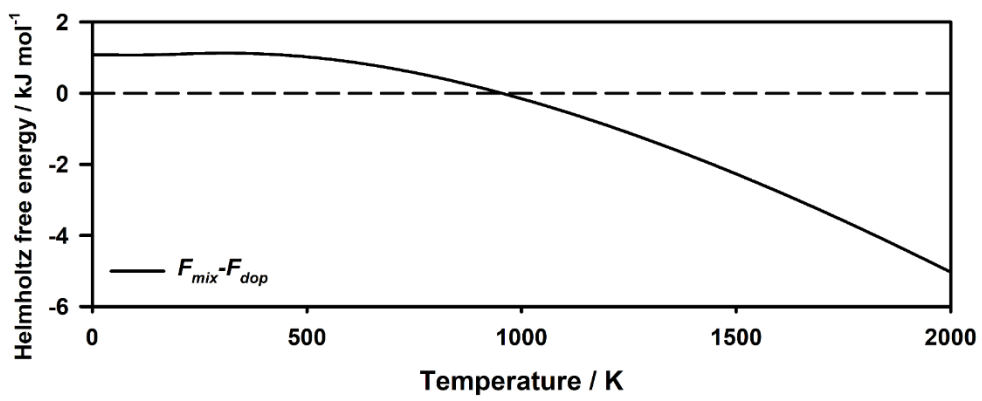


Figure 10. Theoretical Helmholtz free energy difference between $x\text{Li}_2\text{SnO}_3 + (1-x)\text{LiCoO}_2$ (F_{mix}) and $\text{Li}[\text{Sn}_x\text{Co}_{1-x}]\text{O}_2$ (F_{dop}).

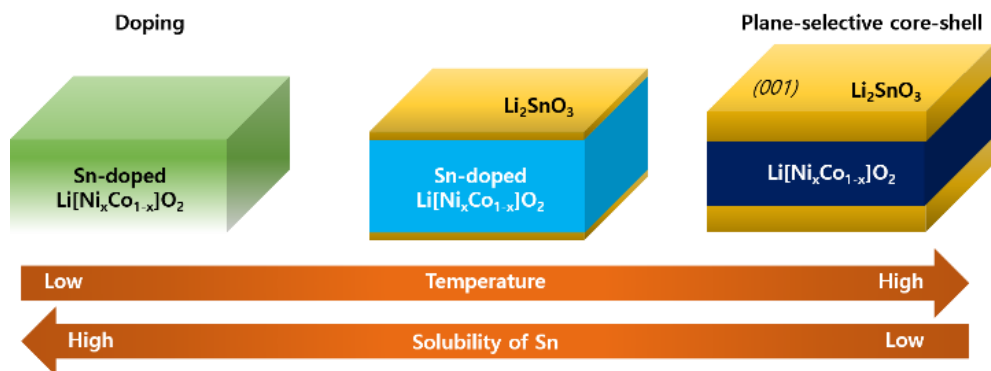


Figure 11. Schematic concept for the synthesis of plane-selectively Li₂SnO₃ coated LiCoO₂.

4.1.2. Phase segregation of Li_2SnO_3 on LiCoO_2

When the sol-gel precursors of LiNO_3 , $\text{Co}(\text{NO}_3)_2 \cdot 6\text{H}_2\text{O}$, SnCl_2 , and citric acid were heated at 700°C , 5 at% Sn-doped LiCoO_2 (space group: $R\bar{3}m$) was obtained without impurities, as shown in its XRD pattern. (**Figure 12**) However, β - Li_2SnO_3 (space group: $C12/c1$) appeared at above 700°C and its XRD peak intensities increased gradually, as the heating temperature increased from 750 to 900°C . This indicates that Sn-doped LiCoO_2 is gradually decomposed to β - Li_2SnO_3 and LiCoO_2 with increasing temperatures at above 700°C . This is further supported by change in the (003) plane peak position of Sn-doped LiCoO_2 with increasing temperatures. The (003) plane peak position of Sn-doped LiCoO_2 obtained at 700°C is lower in 2θ than that of bare LiCoO_2 . This is attributed to that the (003) plane of Sn-doped LiCoO_2 was expanded because of the replacement of Co^{3+} ion (radius: 0.545 Å) with larger Sn^{4+} ion (radius: 0.69 Å) in LiCoO_2 . However, the (003) plane peak position of Sn-doped LiCoO_2 gradually shifted to the higher 2θ with increasing temperatures, and eventually, the XRD peak position of the sample obtained at 900°C is almost same as that of bare LiCoO_2 . This implies that the lattice parameter c of Sn-doped LiCoO_2 decreased with increasing

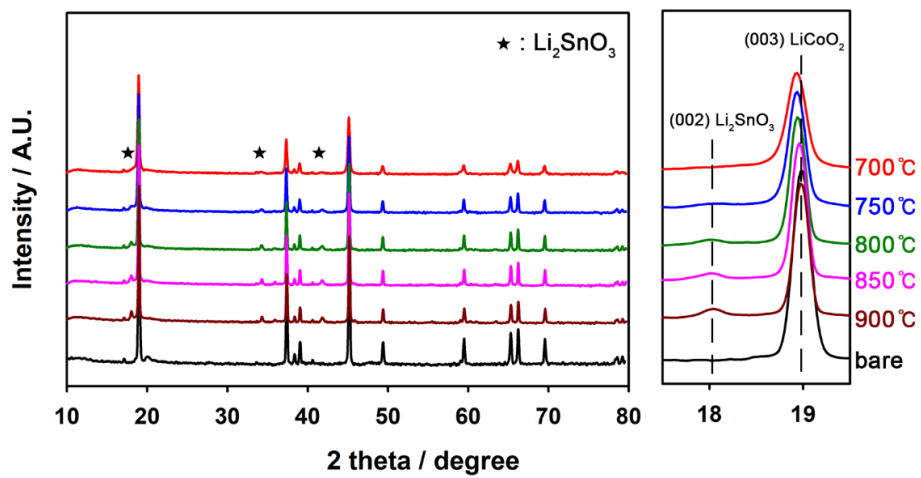


Figure 12. XRD patterns of bare LiCoO₂ and 5 at% Sn added LiCoO₂ at various heating temperatures.

temperatures.

To investigate the change of the lattice parameter and behavior of Sn, the Rietveld refinement was conducted with XRD patterns in **figure 13**. The Rietveld refinement is a powerful tool for analyzing structural information from XRD in that it shows crystallographic information such as space group, lattice parameters, site and occupancies of atoms within a unit cell. As shown in **figure 13**, the Sn amount in a $\text{Li}[\text{Co}_{1-x}\text{Sn}_x]\text{O}_2$ unit cell decreases from 5.00% ($\pm 0.70\%$) to 0.70% ($\pm 0.70\%$) with increasing heating temperature from 700°C to 900°C. In addition, the calculated lattice parameters a and c decreases as the Sn is diffused out from the host material. This reveals that the solubility of Sn in LiCoO_2 decreases with increasing temperature, eventually leading to the phase segregation of Sn-doped LiCoO_2 into a mixture of Li_2SnO_3 and LiCoO_2 at 900°C.

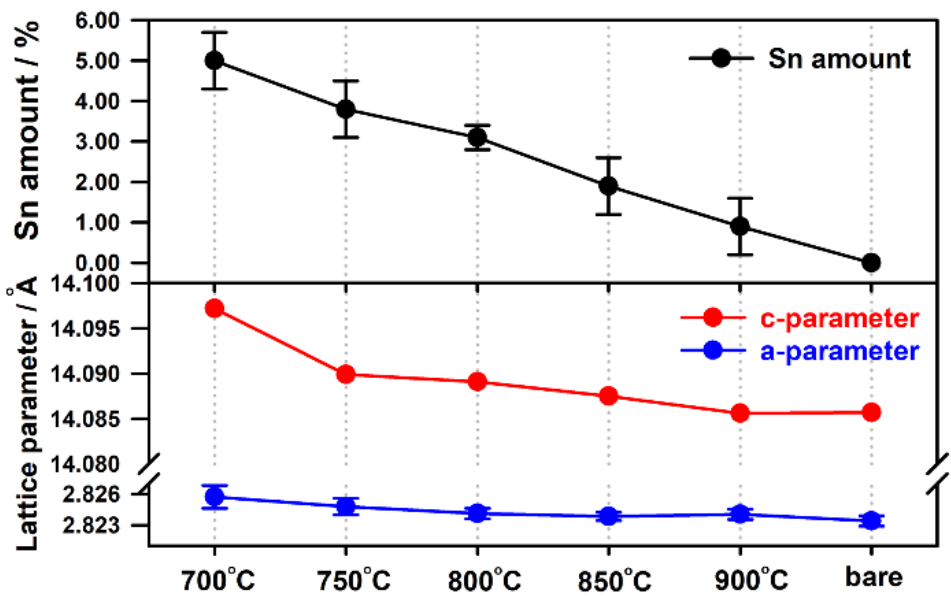


Figure 13. The Rietveld refinement results of XRD patterns in figure 12.

4.1.3. Plane-selective coating of Li₂SnO₃ on LiCoO₂

To investigate morphological change with Li₂SnO₃ segregation on LiCoO₂, scanning electron microscopy(SEM) and cross-section scanning transmission electron microscopy(STEM) images were compared. As shown in **figure 14**, bare, Sn-doped LiCoO₂ and Li₂SnO₃-LiCoO₂ mixture particles are several hundreds of nm in size, with plate morphology in the form of a single crystal. The plate morphology originates from the lower surface energy of (003) plane than other surfaces including (104) and (012) in oxidizing environment.^{85, 86} The high heating temperature gives oxidizing environment during heat treatment.

Cross-sectional STEM analysis was conducted to clarify the phase segregation phenomenon during synthesis. In detail, energy dispersive X-ray spectroscopy (EDS) mapping images were collected to compare the distribution of Sn and Co with respect to heating temperatures. (**Figure 15**) The sample heated at 700°C and 900°C was analyzed as an sample of Sn-doped and Li₂SnO₃-segregated LiCoO₂, respectively. When sample is heated at 700 °C, Sn was uniformly distributed and overlapped with Co within a particle. This result corresponds to the XRD and the Rietveld refinement

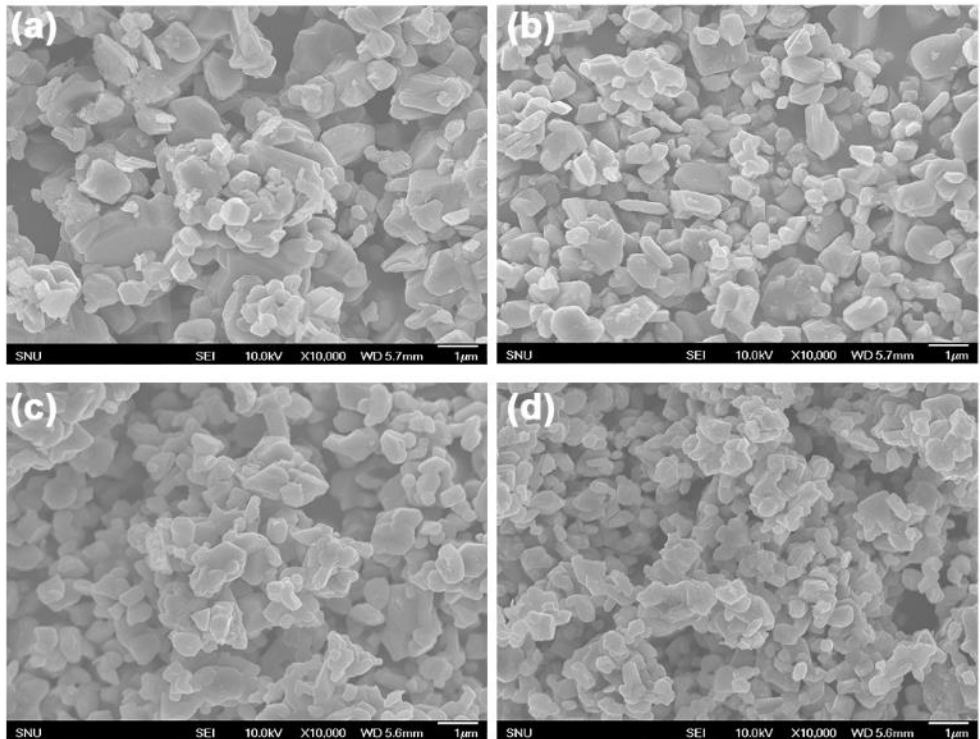


Figure 14. SEM images of $x\text{Li}_2\text{SnO}_3 + (1-x)\text{LiCoO}_2$, where $x =$ (a) 0, (b) 0.01 (c) 0.02 (d) 0.05.

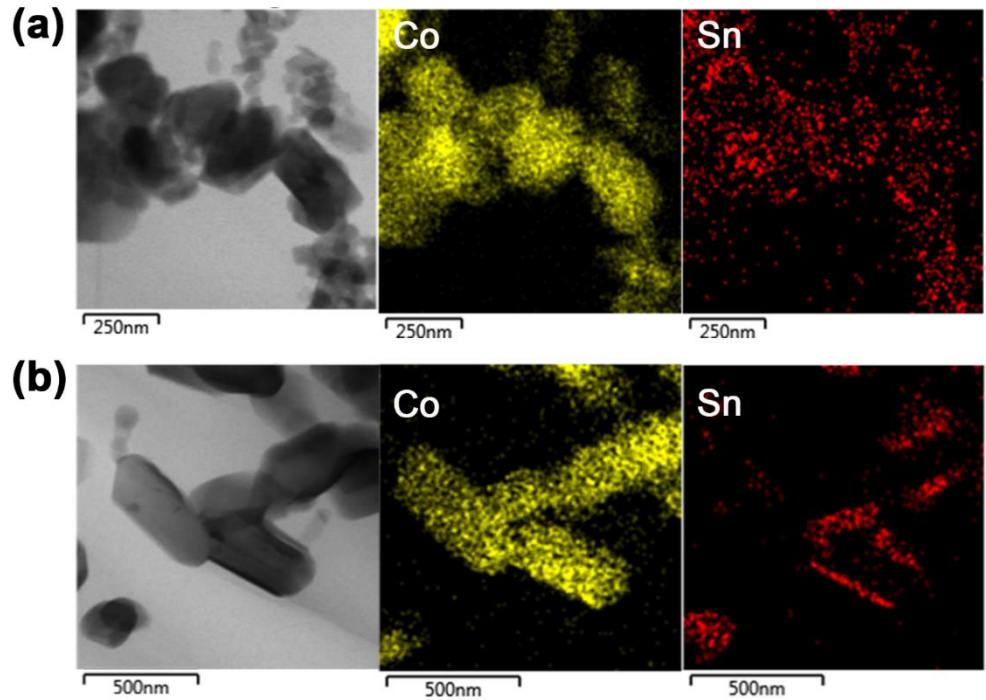


Figure 15. Cross-sectional STEM-EDS mapping images of Sn 5 at% added LiCoO₂ synthesized at (a) 700 and (b) 900 °C, respectively.

result which showed that Sn is successfully doped in LiCoO₂ host structure. At 900°C, however, the distribution region of Sn and Co are clearly separated where Co is located in a particle while Sn in the outside region of a particle. Considering their XRD patterns (**Figure 12**), this suggests that Li₂SnO₃ is segregated outside LiCoO₂ at 900°C. Moreover, it is notable that Li₂SnO₃ does not cover all facets of a LiCoO₂ particle. Li₂SnO₃ layer was selectively and uniformly grown only on the specific plane of LiCoO₂. This selective phase segregation behavior of Li₂SnO₃ was commonly observed throughout all particles. From the cross-sectional line EDS profile along the direction perpendicular to coating layer, the thickness of Li₂SnO₃ coating layer has several tens of nanometers. (**Figure 16**)

To investigate the origin of unique behavior of plane-selective segregation of Li₂SnO₃ on LiCoO₂ at 900°C, the cross-sectional high-angular annular dark-field (HAADF)-STEM images in atomic resolution of the samples with different cooling rates. **Figure 17** shows HAADF-STEM images of the slowly cooled sample. Bright gray and dark gray regions correspond to Li₂SnO₃ and LiCoO₂, respectively. In dark field images, elements with higher atomic number shows brighter images because more electrons are scattered at higher angle due to greater electrostatic interaction between the

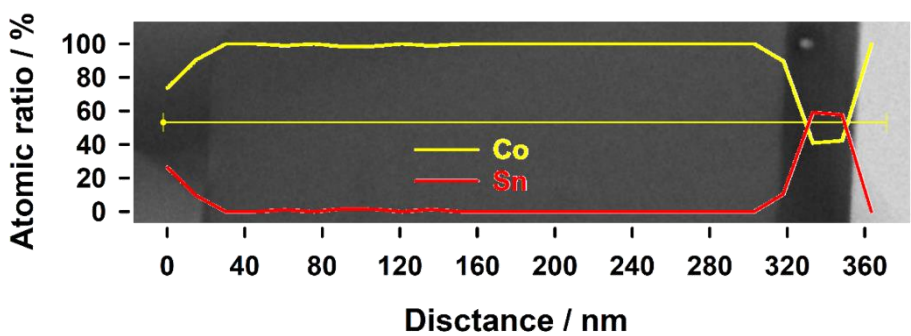


Figure 16. Cross-sectional STEM-EDS line profile of plane-selectively Li_2SnO_3 coated LiCoO_2 .

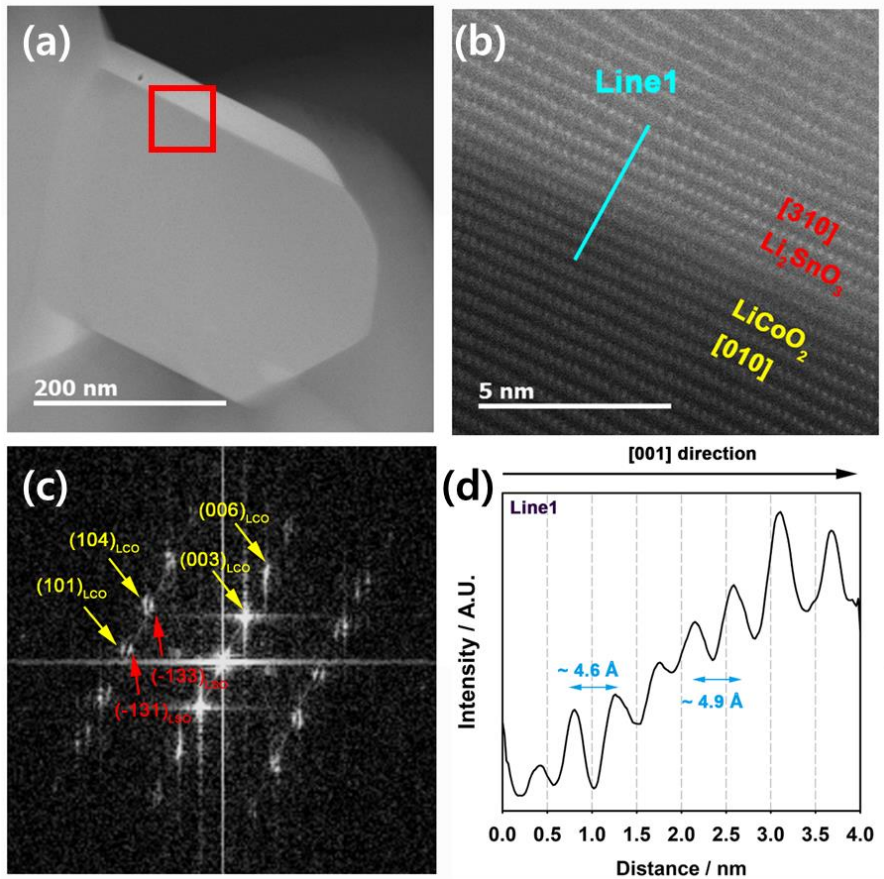


Figure 17. STEM analysis of plane-selectively Li_2SnO_3 coated LiCoO_2 synthesized with slow cooling rate (1/min). (a) Z -contrast image (b) Enlarged Z -contrast image of red square in (a). FFT pattern of (b) image. (d) Line profile of STEM image intensity across the interface through line 1 along [001] direction in (b).

nucleus and the electron beam. As shown in the **figure 17a**, bright region resides only on the specific plane of the particle, indicating that Li_2SnO_3 is segregated only on the specific surface of LiCoO_2 . The magnified atomic resolution image at the interface between Li_2SnO_3 and LiCoO_2 is displayed in **figure 17b**. The magnified image shows the continuous layered structures of Li_2SnO_3 stacked on LiCoO_2 without dislocations. Their corresponding Fast Fourier–Transform (FFT) patterns indicate that the zone–axes of LiCoO_2 and Li_2SnO_3 are [010] and [310], respectively, as shown in **figure 17c**. Since both directions are perpendicular to [001] direction of LiCoO_2 and Li_2SnO_3 , this implies that Li_2SnO_3 coating layers were epitaxially grown on the surface of LiCoO_2 along the [001] direction. To clarify the characteristics at the interface between Li_2SnO_3 and LiCoO_2 , the line profile of image intensity perpendicular to the interface was analyzed through the line 1 along the [001] direction. (**Figure 17d**) The interlayer distances in the dark and the bright regions, respectively, are approximately 4.65 Å and 4.94 Å. They are almost the same as the interlayer distances of LiCoO_2 (4.677 Å, JCPDS #50–0653) and Li_2SnO_3 (4.937 Å, JCPDS #73–0160) along the [001] direction. This indicates that the solubility of Sn in LiCoO_2 is negligible at 900°C, which is consistent with the XRD results. Consequently, this suggests

that, since the solubility of Sn in LiCoO₂ decreases with increasing temperature, Sn-doped LiCoO₂ obtained at 700°C decomposes gradually with further increasing temperature. Eventually, Li₂SnO₃ was grown outside on the surface of LiCoO₂ at 900°C.

For quenched sample, however, the cross-sectional morphology aspect is quite different to the slowly cooled sample. Some of bright regions are located within the particle, indicating that some of Li₂SnO₃ particles are segregated within the LiCoO₂ particle. The interlayer distance is approximately 4.6 Å in the dark region and is 4.9 Å in the bright region. This indicates that the inside domain and the outside area of the quenched sample are Li₂SnO₃ and LiCoO₂, respectively. The different morphology between the slowly cooled and quenched samples suggests that Li₂SnO₃ was diffused out during a slow cooling process, because the (001) surface of Li₂SnO₃ is more stable than that of LiCoO₂.

Moreover, the magnified atomic resolution HAADF image shows that several grain boundaries are generated in quenched sample. (**Figure 18**) In plane-selectively Li₂SnO₃ coated LiCoO₂, the ordered interface is observed perpendicular to the [001] direction. However, the disordered grain boundary was observed at the interface through line 3. This is due to the large lattice mismatch between the Li₂SnO₃

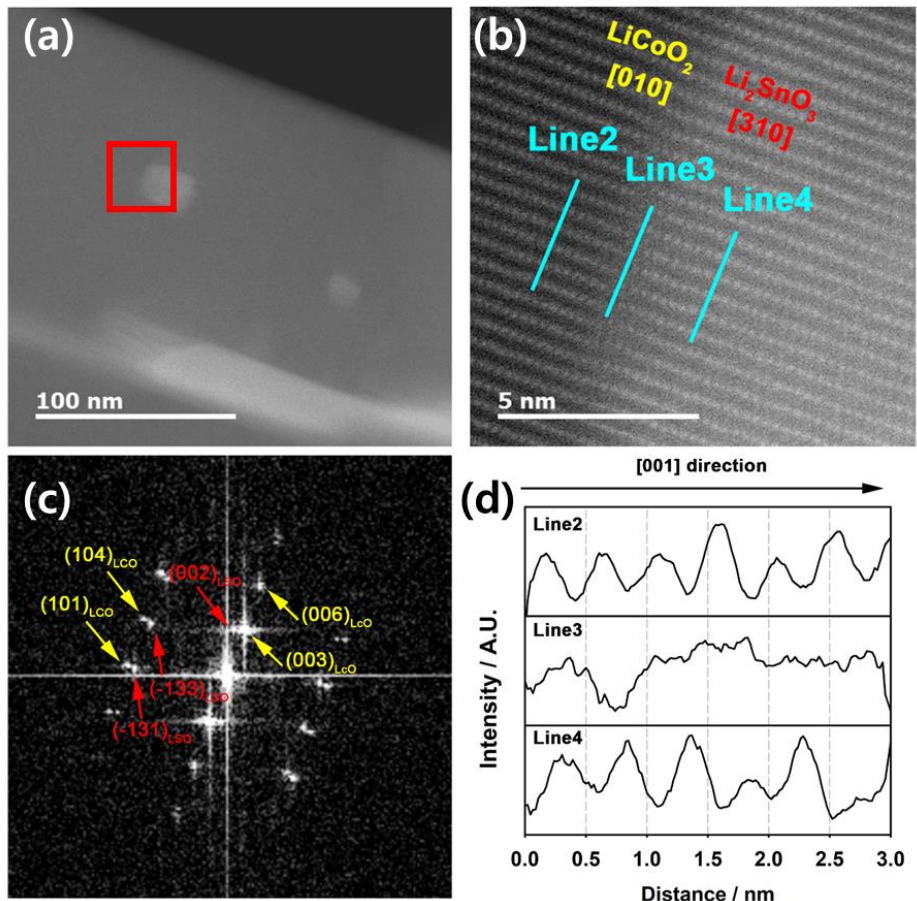


Figure 18. STEM analysis of plane-selectively Li_2SnO_3 coated LiCoO_2 synthesized with quenching. (a) Z-contrast image (b) Enlarged Z-contrast image of red square in (a). FFT pattern of (b) image. (d) Line profile of STEM image intensity across the interface through line 2,3 and 4 along [001] direction in (b), respectively.

and LiCoO_2 planes parallel to the [001] direction. In other words, the epitaxial growth of Li_2SnO_3 is available only on LiCoO_2 planes perpendicular to the [001] direction. The disordered boundary is also generally less stable than the ordered boundary. Therefore, we suggest that the plane-selective growth of Li_2SnO_3 on the LiCoO_2 planes perpendicular to the [001] direction occurs to suppress the disordered boundaries.

4.1.4. Electrochemical performances

To demonstrate the role of the plane-selective Li_2SnO_3 coating on LiCoO_2 in electrochemical performance, the rate and cycle performances of bare, plane-selective Li_2SnO_3 coated LiCoO_2 and conventionally Li_2SnO_3 coated LiCoO_2 were examined. Therefore, the improvement in both rate performance and cycle performance is challenging. XRD pattern of the conventionally Li_2SnO_3 coated LiCoO_2 via sol-gel method shows that there is no structural difference compared with plane-selective Li_2SnO_3 coated LiCoO_2 . (**Figure 19**) Moreover, the conventional sol-gel coating provides randomly covers layered oxide cathode material even where Li^+ ions de-/intercalates, as shown in **figure 20**. Unlike to the plane-

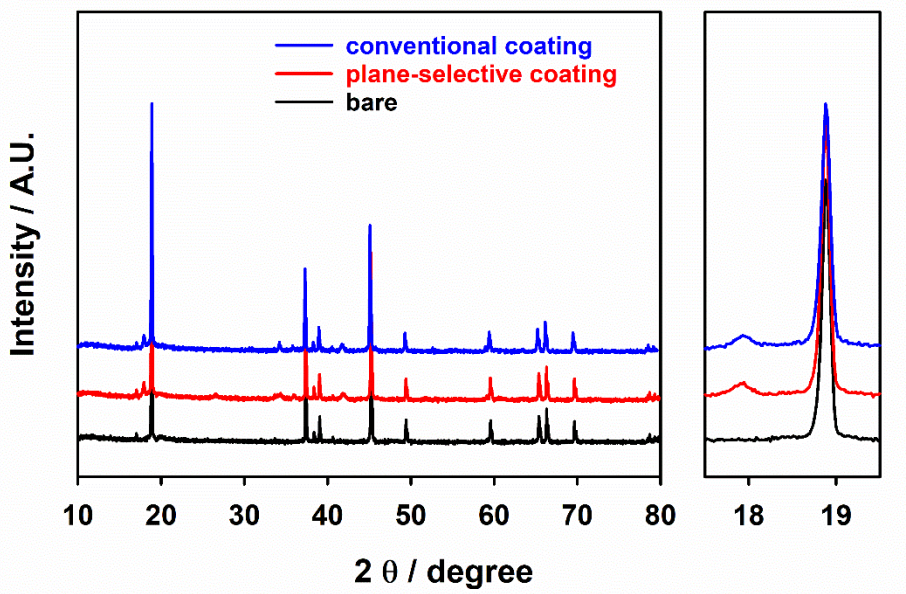


Figure 19. Powder XRD patterns of bare, plane-selectively Li_2SnO_3 coated and conventionally Li_2SnO_3 coated LiCoO_2 .

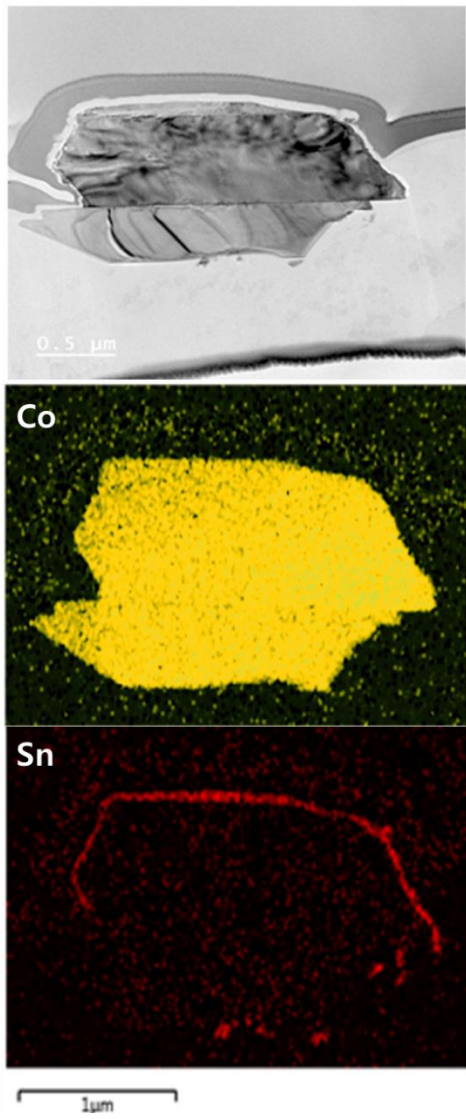


Figure 20. Cross-sectional STEM-EDS mapping images of the sol-gel derived conventionally Li_2SnO_3 coated LiCoO_2 .

selectively Li_2SnO_3 coated LiCoO_2 , Sn is randomly distributed on the surface of the host LiCoO_2 .

The rate performance was evaluated at various C rates from 0.1 (16 mA g⁻¹) to 10 C (1.6 A g⁻¹) rates in the voltage range of 3.0 – 4.5 V (vs. Li/Li⁺). The plane-selective Li_2SnO_3 coated LiCoO_2 showed remarkably better rate performance than did the conventional sol-gel derived Li_2SnO_3 coated LiCoO_2 , as shown in **figure 21**. The discharge capacity retention at 5 C (800 mA g⁻¹) of plane-selectively Li_2SnO_3 coated LiCoO_2 is 81.8 % while that of conventionally Li_2SnO_3 coated LiCoO_2 is 65.2 %. The voltage profiles of plane-selectively and conventionally Li_2SnO_3 coated LiCoO_2 at various C rates are shown in **figure 22**. The polarization of plane-selectively Li_2SnO_3 coated LiCoO_2 are lower than that of conventionally Li_2SnO_3 coated LiCoO_2 at high C rates over 5 C.

Li^+ ions are intercalated and deintercalated into LiCoO_2 through the planes parallel to the [001] direction. (**Figure 23**) The coating layers of the conventional sol-gel derived Li_2SnO_3 coated LiCoO_2 partially cover the charge-transfer planes parallel to the [001] direction, because the conventional coating does not provide plane-selective coating layer. Although Li_2SnO_3 is known as a Li^+ ion conductor, this coating layer still hinders the charge-transfer of Li^+ ions, resulting

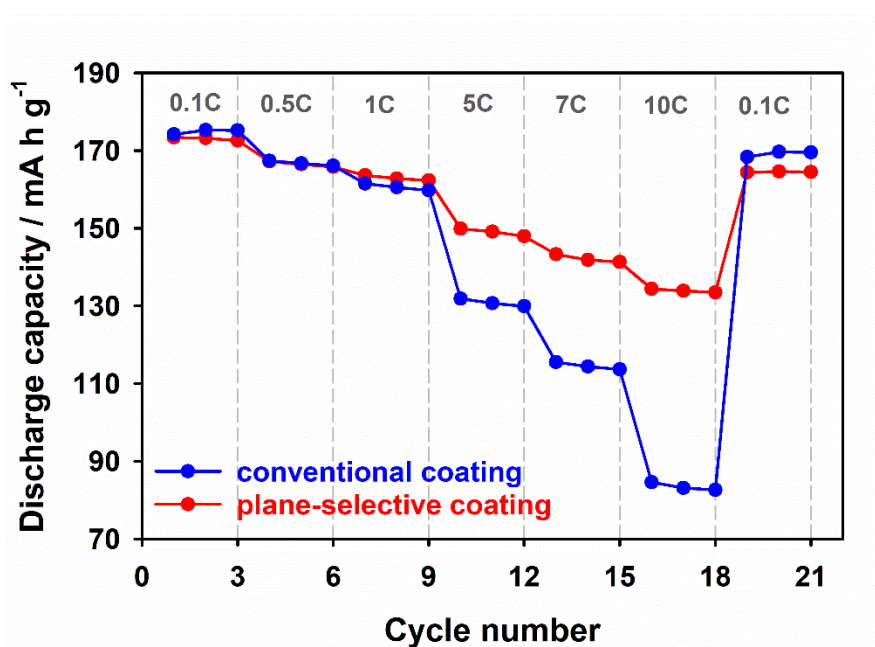


Figure 21. Rate performances of conventionally Li₂SnO₃ coated and plane-selectively Li₂SnO₃ coated LiCoO₂.

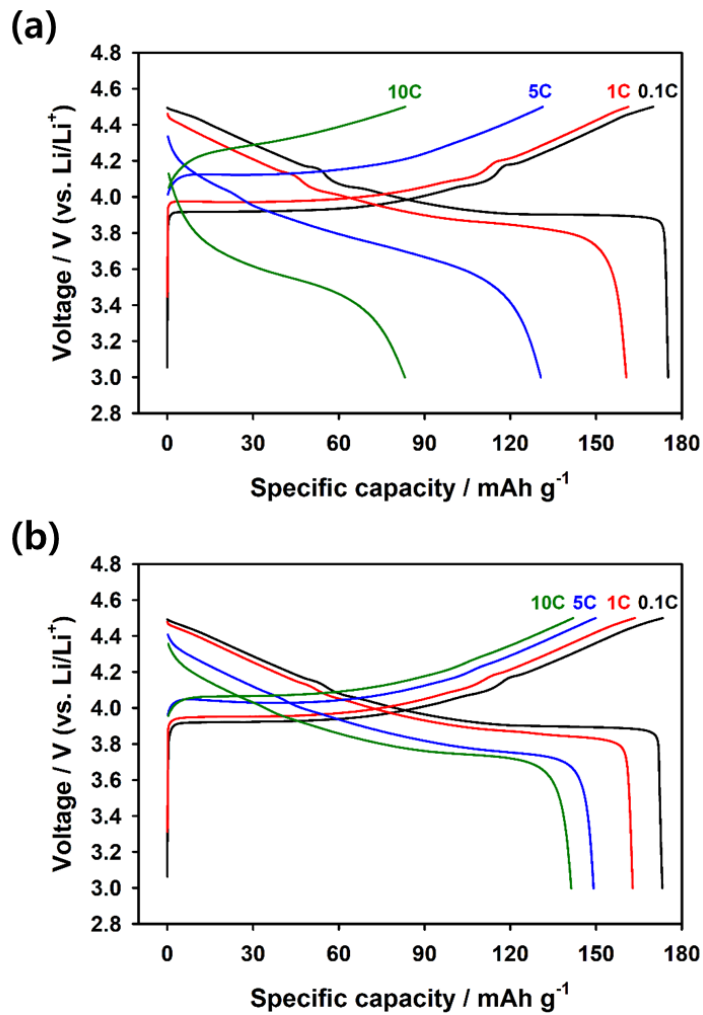


Figure 22. The voltage profiles of (a) conventionally and (b) plane-selectively Li₂SnO₃ coated LiCoO₂ at various C rates.

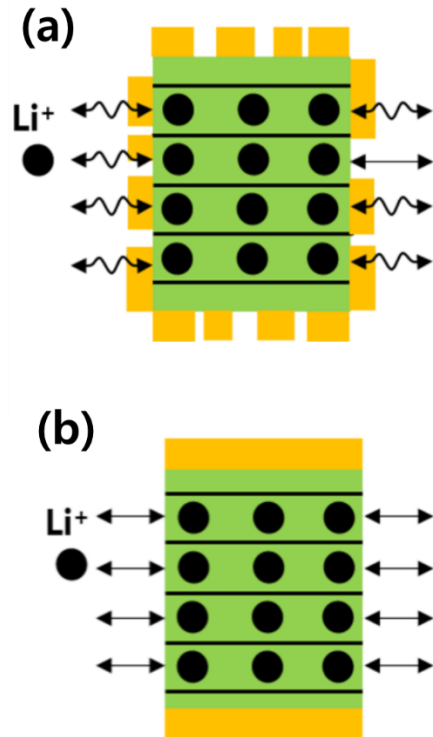


Figure 23. Schematic charge-transfer of Li^+ ions for (a) conventionally Li_2SnO_3 coated LiCoO_2 and (b) plane-selectively Li_2SnO_3 coated LiCoO_2 .

in an increase in charge–transfer resistance. However, the plane–selective Li_2SnO_3 coated LiCoO_2 does not increase charge–transfer resistance, because the Li_2SnO_3 layers are selectively coated only on LiCoO_2 planes perpendicular to the [001] direction, except for the charge–transfer planes.

This is supported by the impedance analysis of cathode/cathode symmetric cells. (**Figure 24**) Each electrode was charged up to 4.5 V under and disassembled and reassembled immediately to prevent self–discharge. The plane–selective Li_2SnO_3 coated LiCoO_2 showed a lower charge–transfer resistance (smaller semicircle) than did the conventionally Li_2SnO_3 coated LiCoO_2 .

The cycle performance of the plane–selective Li_2SnO_3 coated LiCoO_2 was also better than the conventionally Li_2SnO_3 coated LiCoO_2 (**Figure 25**). This suggests that the plane–selective epitaxial coating is more beneficial for suppressing the Co dissolution and irreversible electrolyte decomposition on LiCoO_2 at high voltages (> 4.3 V vs. Li/Li^+) than the conventional sol–gel coating. We speculate that the uniformity of the coated particles is responsible for the enhanced cycle performance. In addition, we examined the electrochemical performance of LiCoO_2 with various coating amounts of Li_2SnO_3 from 1 at% to 5 at%. Even the small coating amount of 1 at% Li_2SnO_3

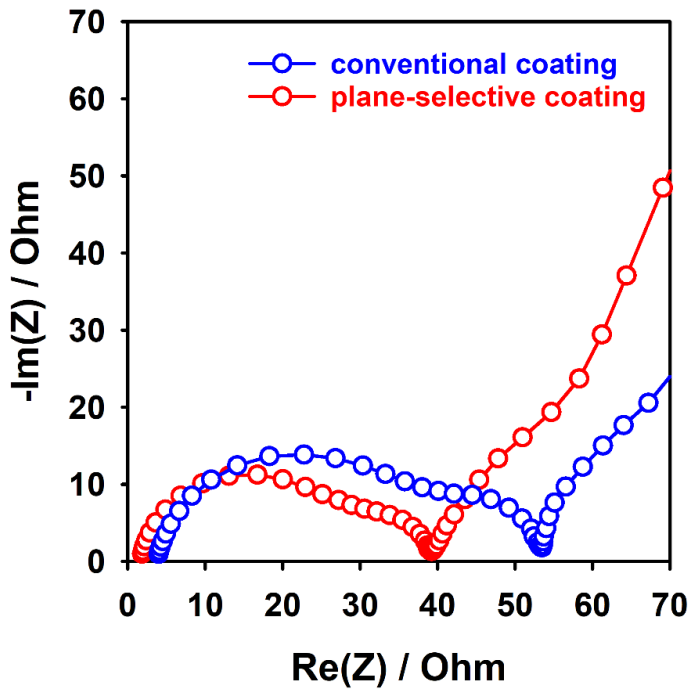


Figure 24. Nyquist plots of $\text{LiCoO}_2/\text{LiCoO}_2$ symmetric cells for conventionally Li_2SnO_3 coated LiCoO_2 and plane-selectively Li_2SnO_3 coated LiCoO_2 .

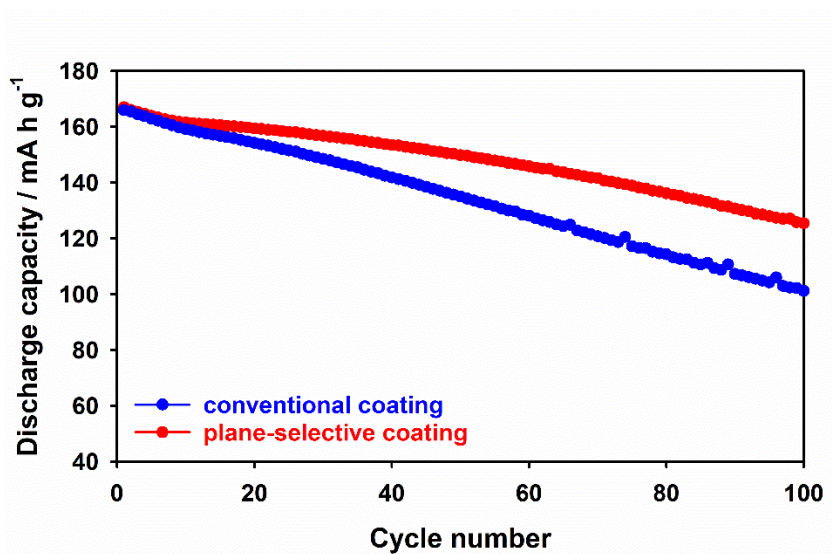


Figure 25. Cycle performance of conventionally Li_2SnO_3 coated LiCoO_2 and plane-selectively Li_2SnO_3 coated LiCoO_2 at 1C rate.

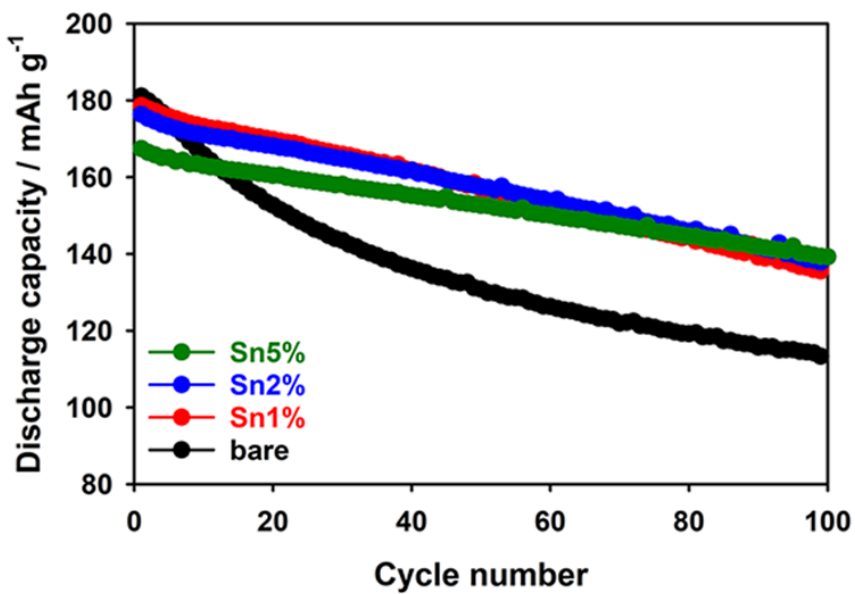


Figure 26. Cycle performances of bare LiCoO_2 and plane-selectively Li_2SnO_3 coated LiCoO_2 with various Sn compositions.

exhibited excellent cycle performance over 100 cycles with a high reversible capacity of 179 mA h g⁻¹ at 1 C rate. (**Figure 26**).

To evaluate effectiveness of plane-selective Li₂SnO₃ coating on LiCoO₂, the storage characteristics at high temperature is examined. (**Figure 27**) The electrodes were charged up to 4.55 V and disassembled in Ar-filled glove box without exposure to H₂O or ambient air. Then, the electrodes were stored in 1.3 M LiPF₆ in EC:EMC:DMC=3:4:3 (v:v:v) for 15 days at 85°C. After storage, the concentration of dissolved Co is examined with ICP-MS. The concentration of dissolved Co ions after high temperature storage greatly reduced in both coated samples. In addition, the concentration of Co is lower in plane-selectively Li₂SnO₃ coated LiCoO₂ than in conventionally Li₂SnO₃ coated LiCoO₂. We speculate that this result is attributed to the denser and conformal coating layer is formed by plane-selective Li₂SnO₃ coating method than conventional coating method.

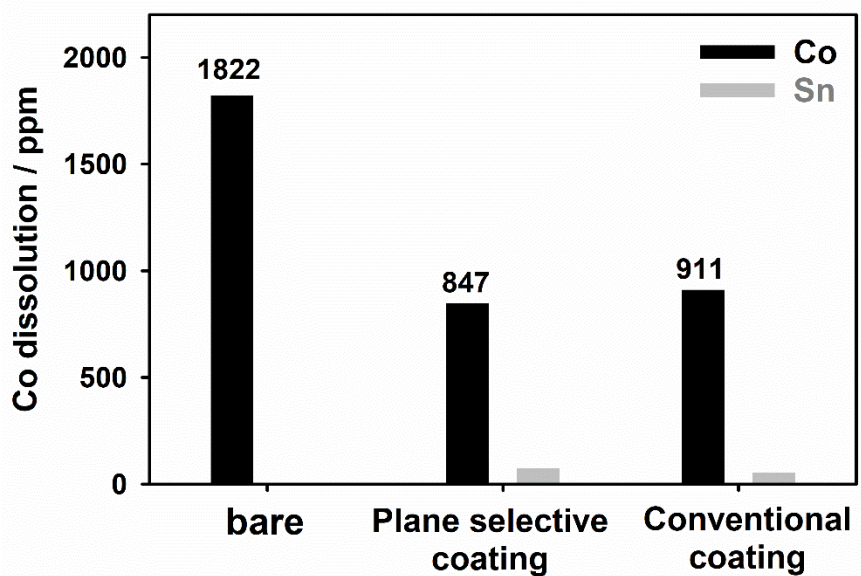


Figure 27. ICP–MS results of dissolved Co ions in electrolyte after storage at 85°C for 15 days.

4.2. Application to Ni-rich layered oxide cathode materials

4.2.1. Phase segregation on $\text{Li}[\text{Ni}_{0.8}\text{Co}_{0.1}\text{Mn}_{0.1}]\text{O}_2$

We have confirmed that one-step plane-selective Li_2SnO_3 coating is an effective method for enhancing electrochemical performances of LiCoO_2 . Although LiCoO_2 shows excellent electrochemical performances, the instability of market price of Co precursor leads to the development of Ni-rich layered oxides. Ni-rich layered oxides can deliver high reversible specific capacity over 200 mAh g^{-1} . However, the surface treatment is inevitable for application of Ni-rich layered oxides due to their reactive surface. Unfortunately, as we discussed in background section, the conventional coating methods, which provides randomly coated morphology, are not effective in enhancing both rate capability and cycle performance. Considering that Ni-rich layered oxide cathode materials exhibits poor rate capability than Co-rich layered oxide cathode materials, it could be more effective to provide one step plane-selective coating layer only on (003) surface of Ni-rich materials in perspective of both cost and electrochemical performances.

We first examined phase segregation temperature of Sn-doped

$\text{Li}[\text{Ni}_{0.8}\text{Co}_{0.1}\text{Mn}_{0.1}]\text{O}_2$ (NCM811) cathode material. The optimized synthesis condition of bare NCM811 is 800°C for 10 hours under O₂ atmosphere. To investigate phase segregation temperature of Sn 2 at% doped NCM811, sol-gel precursors were prepared following procedures in experimental section 3.1.2. Then, the powders were heated at 800°C for 9 hours followed by heat treatment at 860, 880 and 900°C for 10 minutes then slowly cooled (1°C/min) to room temperature. This 2 step heat treatment is to minimize the structural deterioration at high synthesis temperature. In detail, it is reported that LiNiO₂ decomposes into $\text{Li}_{1-x}\text{Ni}_{1+x}\text{O}_2$ ($x > 0$) at high temperature over optimized temperature ($> 700^\circ\text{C}$). At higher temperature, LiNiO₂ is believed to be decomposes into $\text{Li}_{1-x}\text{Ni}_{1+x}\text{O}_2$, Li₂O and gaseous O₂. In oxidizing condition like O₂ atmosphere, Li₂O easily transforms into Li₂O₂.⁸⁷ This indicates that the chemical delithiation occurs during synthesis at high synthesis temperature, which facilitates the migration of Ni ions into Li layer. Therefore, a careful consideration is needed to be addressed on the optimization of synthesis temperature of Ni-rich layered oxides.

Figure 28 shows the powder XRD patterns of bare and Sn 2 at% added NCM811 powders synthesized at various heating temperature. Regardless of synthesize temperature, all NCM811 samples show *R*-

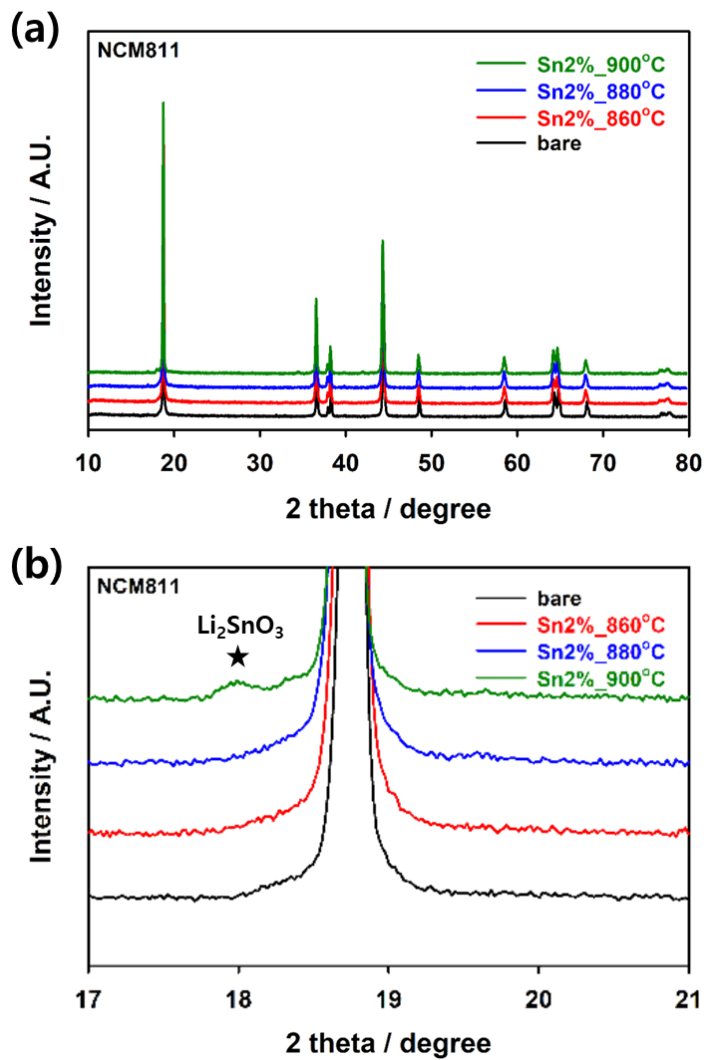


Figure 28. The XRD patterns of Sn 2 at% added

$\text{Li}[\text{Ni}_{0.8}\text{Co}_{0.1}\text{Mn}_{0.1}]\text{O}_2$ synthesized at various temperatures.

β m layered structure. From magnified XRD pattern in region between 17–20°, (002) peak of Li_2SnO_3 around 18° is observed for the sample synthesized at 900°C. The peak shift of (003) NCM811 around 18.9° was negligible in XRD pattern, which is attributed to the small amount of Sn concentration changed within the host material.

To clarify the structural change with heating temperature, the Rietveld refinement was conducted. As shown in **figure 29**, bare NCM811 shows 1.8 % of cation disorder at the optimized synthesis temperature. For Sn 2 at% added NCM811, the amount of doped Sn^{4+} ion is 2.0, 0.9 and 0.5% as the heating temperature increases from 860, 880 and 900°C, respectively. This result is consistent with the Li_2SnO_3 – LiCoO_2 phase segregation phenomenon, discussed in previous section. Although it is confirmed that the phase segregation with increasing heating temperature between Li_2SnO_3 and NCM811 is possible, the structural deterioration is observed for NCM811. The cation disorder of NCM811 host material is 2.3, 2.5 and 2.7 % at 860, 880 and 900°C, respectively. This structural deterioration leads to the deterioration of electrochemical performance, which will be discussed later in this study.

To investigate the phase segregation morphology of Li_2SnO_3 segregated NCM811, cross-sectional STEM–EDS mapping analysis

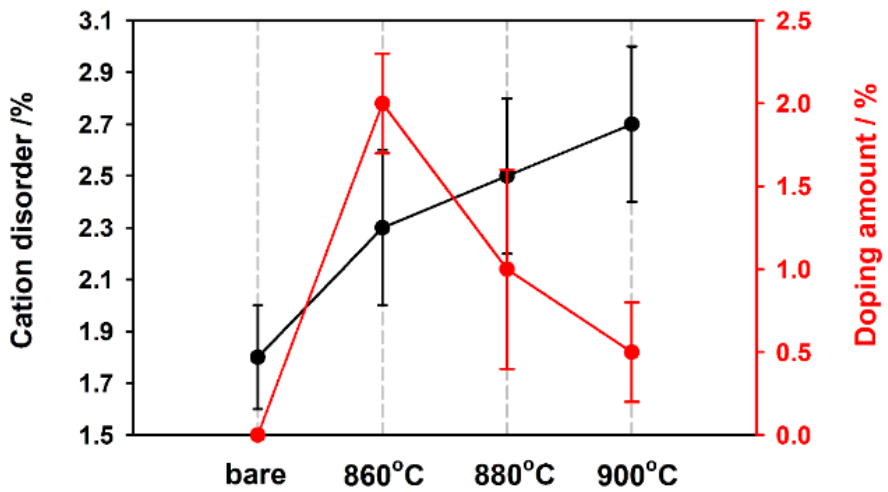


Figure 29. Rietveld refinement results of XRD patterns in figure 28.

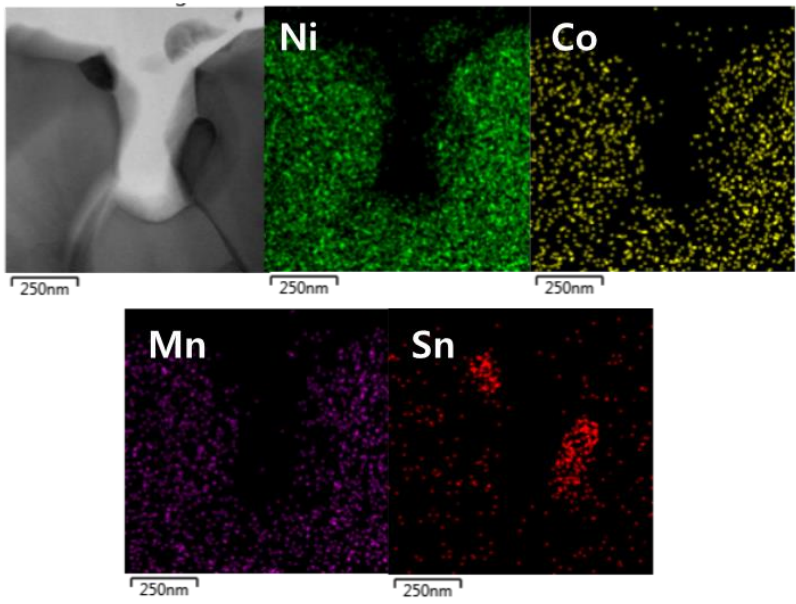


Figure 30. Cross-sectional STEM-EDS mapping images of Sn 2 at% added Li[Ni_{0.8}Co_{0.1}Mn_{0.1}]O₂ synthesized at 900 °C.

was conducted for the sample synthesized at 900°C. As shown in the **figure 30**, Ni, Co and Mn are homogenously distributed throughout the particle. Interestingly, the Sn is segregated on the surface of NCM811 particle. Unfortunately, however, unlike (003) plane-selective Li₂SnO₃ coating layer is observed in LiCoO₂, Li₂SnO₃ coating layer is not segregated on (003) surface of NCM811. The Li₂SnO₃ coating layer is randomly distributed on the surface of NCM811 particles. The origin of random distribution of Li₂SnO₃ coating layer will be discussed in layer section in detail.

Due to the random distribution of Li₂SnO₃ coating layer and structural deterioration during phase segregation, one-step phase segregation coating of Li₂SnO₃ on NCM811 does not significantly enhance electrochemical properties of NCM811 active material, as shown in **figure 31**. Bare NCM811 shows discharge capacity of 199.7 mAh g⁻¹ while the discharge capacity decreases from 189.3, 184.0 and 176.6 mAh g⁻¹ with increasing heating temperature from 860, 880 and 900°C, respectively.

Moreover, the polarization at initial charge step increases with increasing heating temperature, exhibiting great increase in polarization in the sample synthesized at 900°C. (**Figure 32**) The increase in polarization at the initial charge is closely related to the

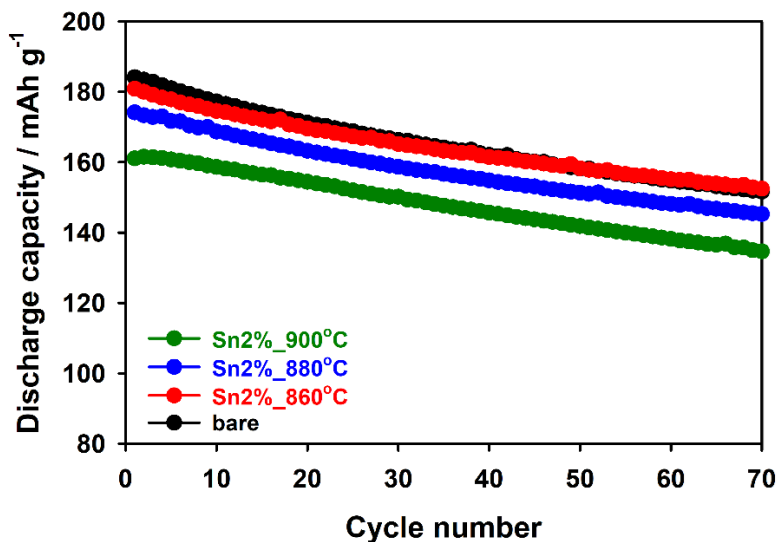


Figure 31. Cycle performances of bare $\text{Li}[\text{Ni}_{0.8}\text{Co}_{0.1}\text{Mn}_{0.1}]\text{O}_2$ and Sn 2 at% added $\text{Li}[\text{Ni}_{0.8}\text{Co}_{0.1}\text{Mn}_{0.1}]\text{O}_2$ synthesized at various temperatures.

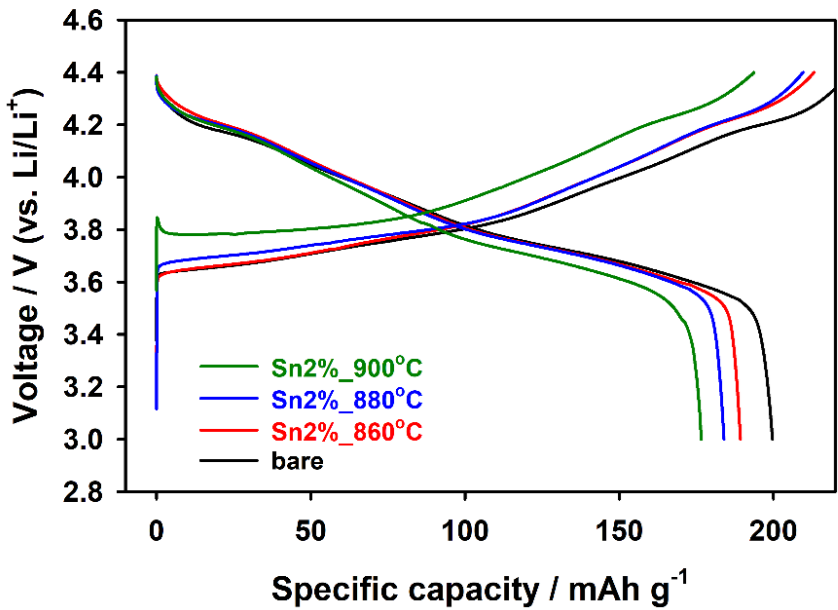


Figure 32. Voltage profiles of formation cycles of bare $\text{Li}[\text{Ni}_{0.8}\text{Co}_{0.1}\text{Mn}_{0.1}]\text{O}_2$ and Sn 2 at% added $\text{Li}[\text{Ni}_{0.8}\text{Co}_{0.1}\text{Mn}_{0.1}]\text{O}_2$ synthesized at various temperatures.

value of cation disorder in Ni-rich layered oxide cathode materials. The cation disorder represents the amount of Ni^{2+} ions in the Li layer, which act as pillar that hinders Li^+ ion diffusion within the Li slab. In this way, the reduced Li^+ ion mobility within the diffusion layer results in the increase of polarization during charge and discharge. In addition to the increase in polarization with increasing temperature, randomly Li_2SnO_3 coated NCM811 does not exhibit superior cycle performance than bare NCM811. According to the fact that the degree of cation disorder increases with increasing heating temperature in Sn added NCM811 as we discussed in **figure 29**, it is speculated that the increased heating temperature for phase segregation of Li_2SnO_3 is responsible for the degradation in electrochemical performances.

We speculate that the increase of heating temperature needed to phase segregation arises from the dopant–host material chemistry. It is reported that there are two limiting factors that affects the dopant solubility limit in a host material– (i) the difference in ionic radius between dopant and host ion and (ii) the difference in oxidation state of dopant and host ion.⁸⁸ This concept was proposed by Z.Ogumi group in the case study of dopant–host chemistry of various dopants and LiCoO_2 with computational method. In general, the solubility of

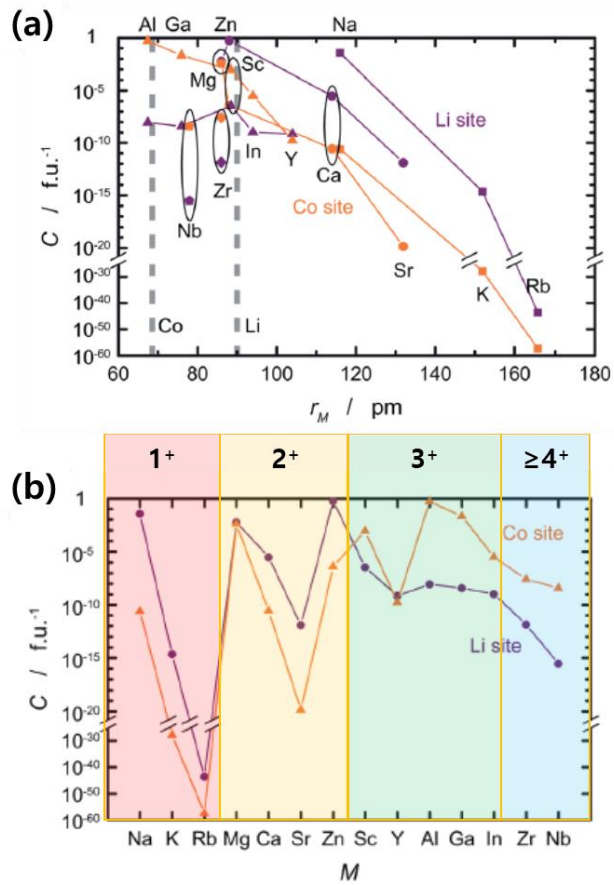


Figure 33. Two limiting factors that determining the solubility limit of dopants. The relationship between (a) ionic radius of dopants and (b) oxidation state of dopants.⁸⁸

the dopant increases as the difference in the ionic radius between the dopant and the host ion decreases. In layered oxide cathode materials, the Ni^{3+} , Co^{3+} and Mn^{4+} ions are known to prevail the transition metal layer where their ionic radius are 0.56, 0.545 and 0.54 Å, respectively. The difference in ionic radii between Sn^{4+} (0.69 Å) and host ions is around 0.15 Å, exhibiting negligible difference between the host transition metal ions. However, considering that the phase segregation between Li_2SnO_3 and LiCoO_2 occurred over 700°C while that between Li_2SnO_3 and NCM811 occurred over 860°C, the difference of ionic radius between Sn^{4+} and host transition metal ion is not the limiting factor that determine the solubility limit of Sn^{4+} ion in layered oxide cathode material.

The other remaining limiting factor is the similarity in oxidation state of Sn^{4+} and host ions. The oxidation state of host ion (Co) is 3+ in LiCoO_2 while that of host ion is known to vary according to the composition of Ni, Co, and Mn. In high Ni–composition *ca.* $\text{Li}[\text{Ni}_{0.8}\text{Co}_{0.1}\text{Mn}_{0.1}]\text{O}_2$, the oxidation state of Ni, Co and Mn is known to be 2+, 3+ and 4+, respectively. The presence of Mn^{4+} can increase the solubility limit of Sn^{4+} in NCM811 in that it increases concentration of Ni^{2+} in a host material which has similar ionic radius with Sn^{4+} ions.

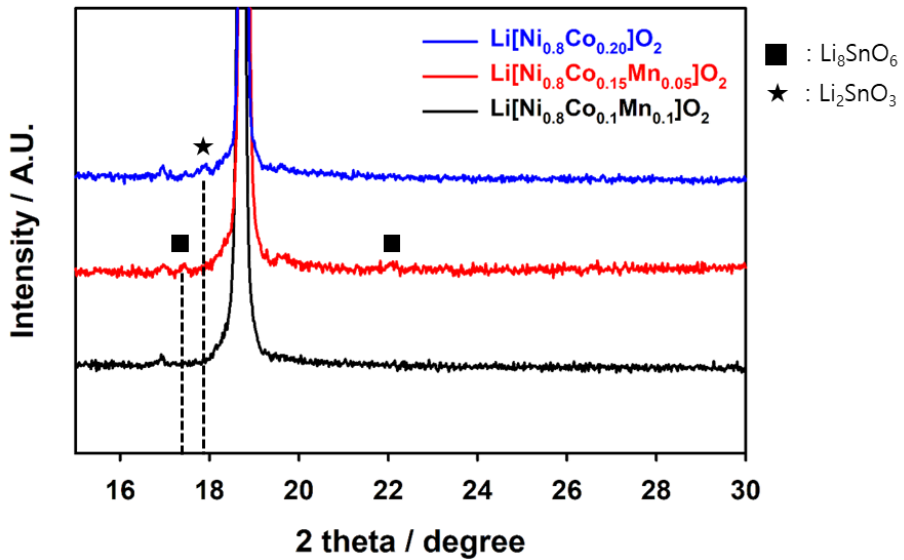


Figure 34. XRD patterns of Sn 2 at% added $\text{Li}[\text{Ni}_{0.8}\text{Co}_{0.1+x}\text{Mn}_{0.1-x}]\text{O}_2$ ($x=0, 0.05, 0.1$) synthesized at 800 °C

To clarify the effect of Mn⁴⁺ in NCM811 phase segregation, Sn 2% added Li[Ni_{0.8}Co_{0.1+x}Mn_{0.1-x}]O₂ (x=0, 0.05 and 0.1) were synthesized at the same heating temperature at 800 °C. As shown in the **figure 34**, no additional peak is observed for Li[Ni_{0.8}Co_{0.1}Mn_{0.1}]O₂. However, the additional peaks of Li₈SnO₆ and Li₂SnO₃ are observed with the decrease Mn composition to 5% to 0, respectively. Considering that the Li/Sn ratio in Li₈SnO₆ is 8 and that in Li₂SnO₃ is 2, as Mn composition increases, it is confirmed that the amount of Sn diffused out from the host material and phase segregated on the surface increases.

This fact is supported by the cross-sectional STEM-EDS mapping results of Li[Ni_{0.8}Co_{0.2}]O₂ and Li[Ni_{0.8}Co_{0.1}Mn_{0.1}]O₂. (**Figure 35**) The phase segregated Li₂SnO₃ is coated on the random surfaces of Li[Ni_{0.8}Co_{0.2}]O₂. However, Sn is homogenously doped in Li[Ni_{0.8}Co_{0.1}Mn_{0.1}]O₂ synthesized at the same temperature. These findings suggest that reducing Mn composition is essential for phase segregation coating for Ni-rich layered oxide cathode materials.

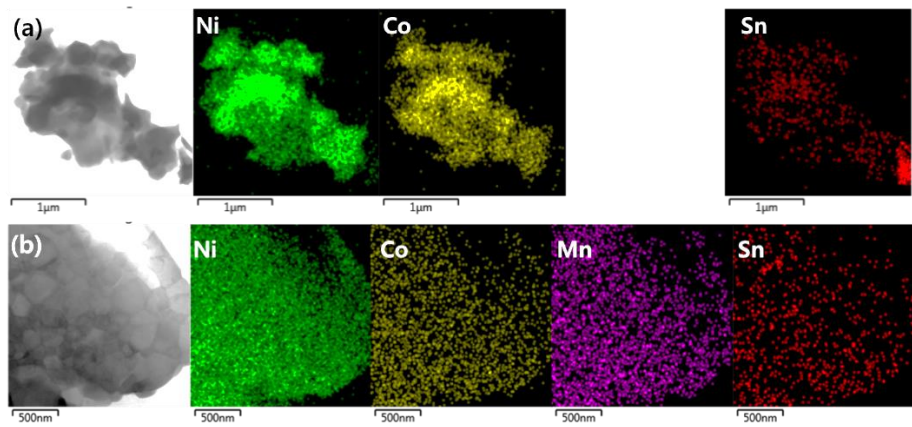


Figure 35. Cross-sectional STEM-EDS mapping images of Sn 2 at% added (a) $\text{Li}[\text{Ni}_{0.8}\text{Co}_{0.2}]\text{O}_2$ and (b) $\text{Li}[\text{Ni}_{0.8}\text{Co}_{0.1}\text{Mn}_{0.1}]\text{O}_2$ synthesized at 800 °C.

4.2.2. Phase segregation on Li[Ni_{0.80}Co_{0.15}Al_{0.05}]O₂

Based on the above research results, it was confirmed that the one-step phase segregation coating method is not effective in the Ni-rich NCM811 material due to the structural deterioration issue arise from the increase in the heat temperature, which leads to the increase in the solubility of Sn⁴⁺ ions in presence of Mn⁴⁺ ions. Therefore, alternative Mn-free Ni-rich layered oxide material should be considered as a host material. Ni-rich Li[Ni_{0.80}Co_{0.15}Al_{0.05}]O₂ (NCA) material is one of the promising Ni-rich layered cathode materials for Li ion batteries. Due to the introduction of Al³⁺ ions, NCA material exhibits low degree of cation disorder during synthesis and cycling, which leads to stable cycle performance and rate performance.

To investigate the phase segregation behavior in NCA host material, Sn 5 at% added NCA and NCM811 were synthesized via sol-gel method. The optimized synthesis temperature of bare NCA material is known to 750°C. As shown in **figure 36**, (002) peak of Li₂SnO₃ is observed in Mn-free NCA material synthesized at 750°C which is the same with the bare NCA synthesis temperature. Moreover, with the rise of (002) peak of Li₂SnO₃ with increasing heating temperature, the (003) peak of NCA shifts to higher diffraction angle, indicating

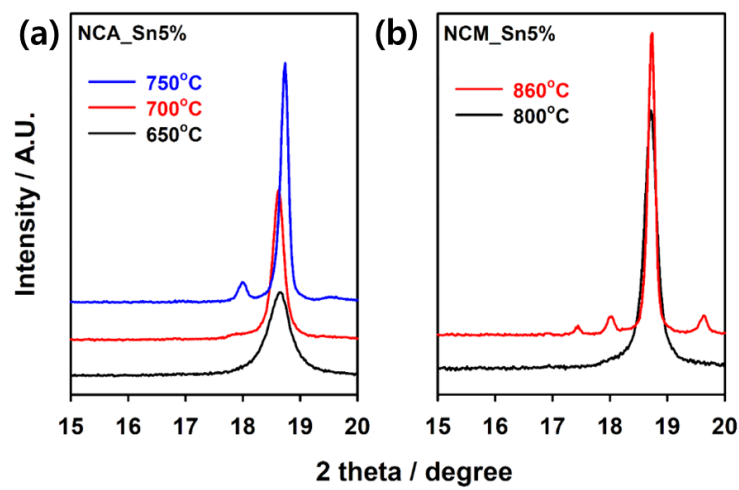


Figure 36. XRD patterns of Sn 5 at% added (a)

$\text{Li}[\text{Ni}_{0.80}\text{Co}_{0.15}\text{Al}_{0.05}]\text{O}_2$ and (b) $\text{Li}[\text{Ni}_{0.8}\text{Co}_{0.1}\text{Mn}_{0.1}]\text{O}_2$ synthesized at various temperatures.

that Sn ions are diffused out from the host NCA material to form Li_2SnO_3 . However, the XRD pattern of Sn 5% added NCM811 material shows that the phase segregation of Li_2SnO_3 occurs on the temperature over 860°C which is beyond the optimized synthesis temperature for bare NCM811 (800°C).

To clarify the structural change during synthesis in NCA and NCM811, the Rietveld refinement was conducted for bare and phase segregated samples. As shown in **figure 37**, NCM811 material shows higher degree of cation disorder at 860°C (2.1%) where the temperature Li_2SnO_3 phase segregation occurs than the bare 811 material (1.8%). On the other hand, NCA material shows negligible change in degree of cation disorder at the temperature where Li_2SnO_3 phase segregation occurs. These structural analyses results imply that the NCA material is more appropriate than NCM811 material for the one-step phase segregation coating for Ni-rich layered oxide cathode material.

To investigate the morphology of Li_2SnO_3 phase segregated NCA material, cross-sectional STEM-EDS mapping analysis was conducted. As shown in the **figure 38**, Sn is located at separated region with host ions such as Ni and Co. However, similar to NCM811 material, the Li_2SnO_3 coating layer is not plane-selectively

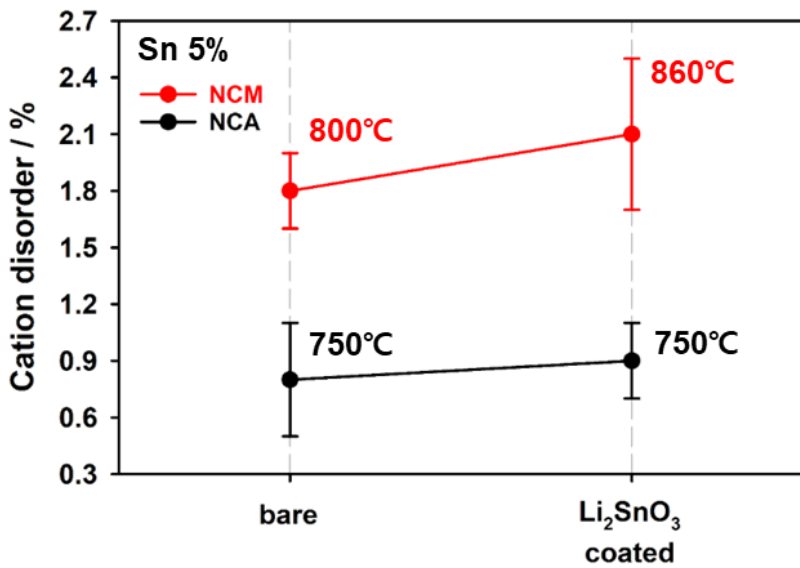


Figure 37. The Rietveld refinement results of bare and Sn 5 at% added $\text{Li}[\text{Ni}_{0.80}\text{Co}_{0.15}\text{Al}_{0.05}]\text{O}_2$ and $\text{Li}[\text{Ni}_{0.8}\text{Co}_{0.1}\text{Mn}_{0.1}]\text{O}_2$ at various temperatures.

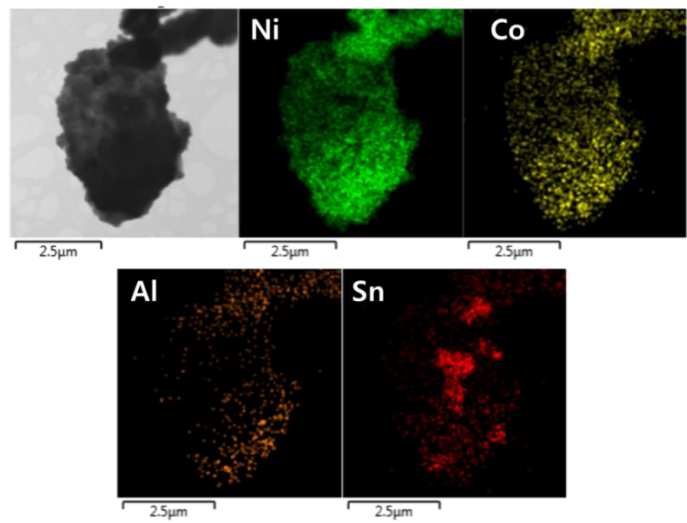


Figure 38. Cross-sectional STEM-EDS mapping images of Sn 5 at% added Li[Ni_{0.80}Co_{0.15}Al_{0.05}]O₂ synthesized at 750 °C.

segregated on the host material. We speculate that the origin of the random segregation of Li_2SnO_3 is closely related with the particle morphology of the host materials.

In case of LiCoO_2 in which plane-selective Li_2SnO_3 coating layer is formed, the host LiCoO_2 material shows plate-like single crystal morphology, as shown in **figure 39**. The plate-like single crystalline morphology of LiCoO_2 results in the large areal exposure of (003) surface which can act as substrate for Li_2SnO_3 coating layer. However, the Ni-rich layered oxides exhibit randomly shaped morphology regardless of the composition of other elements such as Co, Mn and Al. (**Figure 40**) Therefore, controlling the morphology of the host material is a crucial factor for plane-selective coating of Li_2SnO_3 .

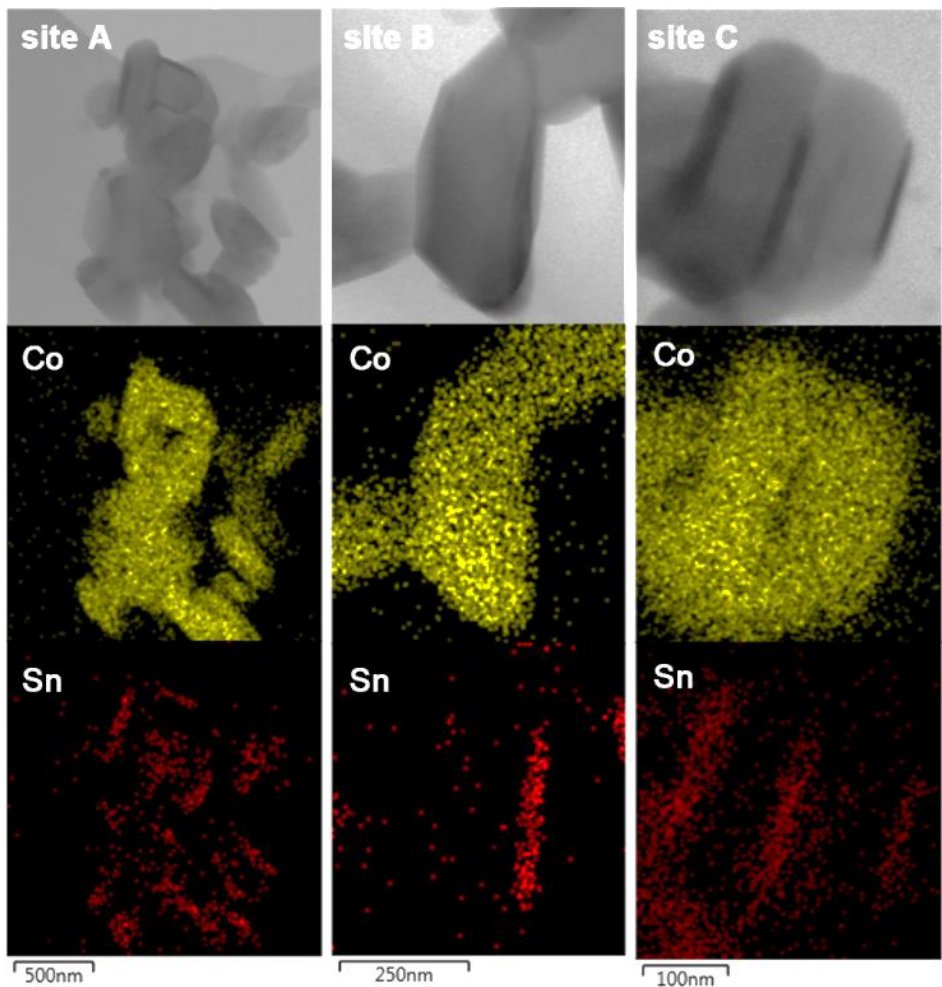


Figure 39. Cross-sectional STEM-EDS mapping images of plane-selectively Li_2SnO_3 coated LiCoO_2 at various sites.

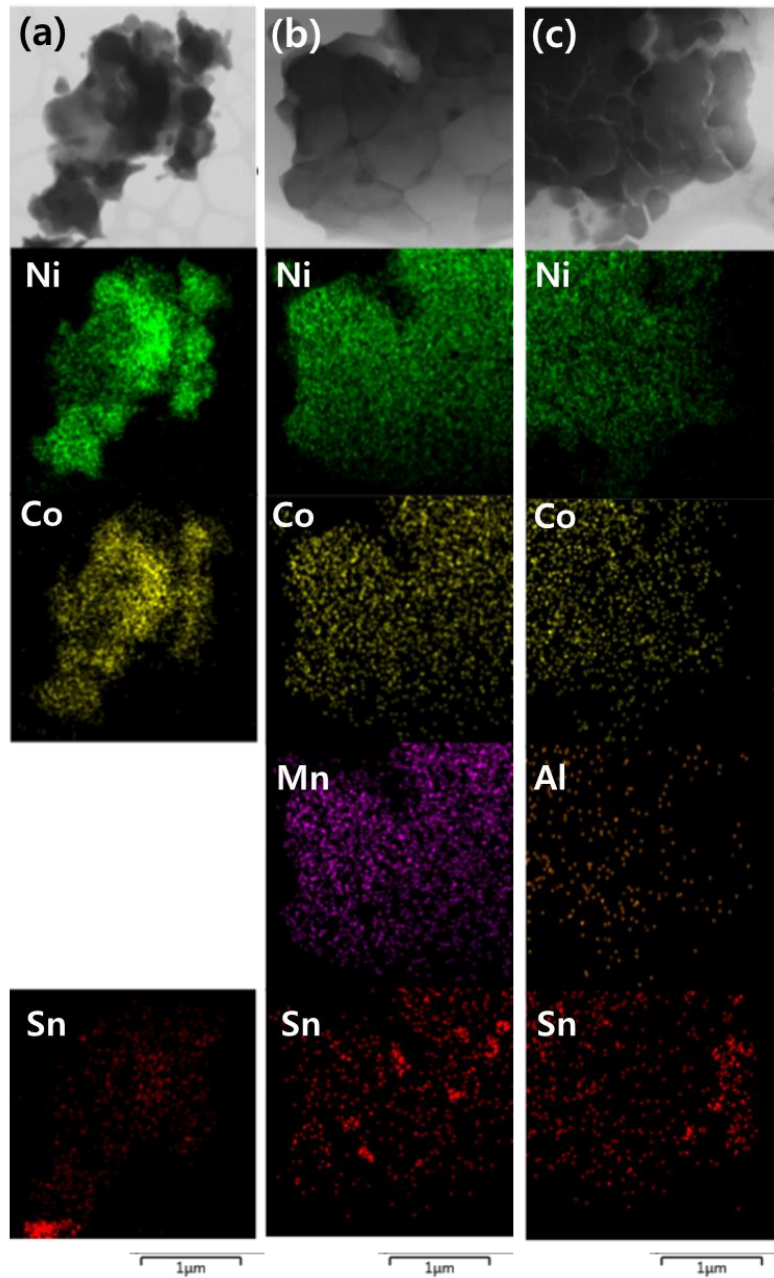


Figure 40. Cross-sectional STEM-EDS mapping images 5 at% Li_2SnO_3 segregated on (a) $\text{Li}[\text{Ni}_{0.8}\text{Co}_{0.2}]\text{O}_2$ (b) $\text{Li}[\text{Ni}_{0.8}\text{Co}_{0.1}\text{Mn}_{0.1}]\text{O}_2$ and (c) $\text{Li}[\text{Ni}_{0.80}\text{Co}_{0.15}\text{Al}_{0.05}]\text{O}_2$.

4.2.3. Plane-selective Li₂SnO₃ coating on Li[Ni_{0.80}Co_{0.15}Al_{0.05}]O₂ through hydrothermal synthesis

To provide plate-like morphology of NCA material, as we discussed in previous section, precursor of $[Ni_{0.80}Co_{0.15}Al_{0.05}]_{0.95}Sn_{0.05}(OH)_2$ was synthesized via hydrothermal method. As shown in TEM-EDS mapping images in **figure 41**, Sn 5 at% doped $[Ni_{0.80}Co_{0.15}Al_{0.05}]_{0.95}(OH)_2$ shows flake-type morphology with homogenous distribution of Ni, Co and Sn throughout the particle. Solid-state synthesis was conducted with the mixing LiOH•H₂O and the synthesized precursor. As shown in **figure 42**, (002) peak of Li₂SnO₃ gradually increases with increasing heating temperature until 750°C, accompanied by the peak shift of (003) peak of NCA to higher diffraction angle. This result is consistent with the XRD results discussed in previous sections. Moreover, at 780 °C, the presence of Li₈SnO₆ is observed with peak shift of (003) peak of NCA to lower angle. This result implies that the diffusion rate of Li⁺ is higher than that of Sn⁴⁺ over 780°C, which can lead to the deterioration of the host material.

To investigate the structural changes during synthesis, the Rietveld refinement was conducted. As shown in **figure 43**, Sn 5% doped NCA

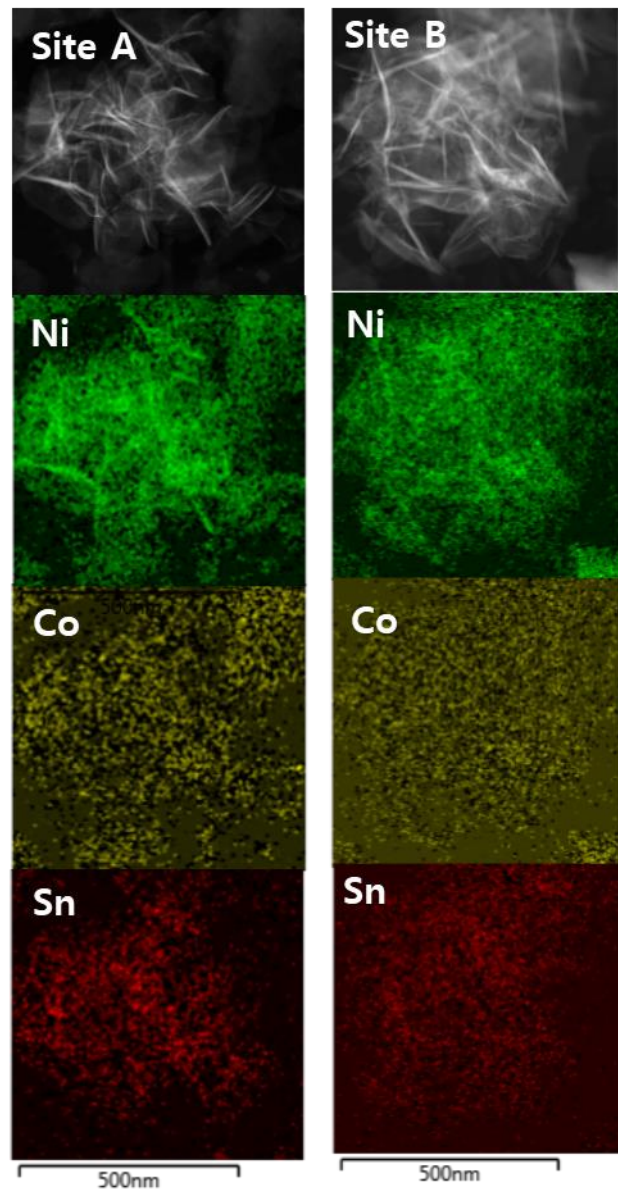


Figure 41. TEM-EDS mapping images of Sn 5 at% added $[Ni_{0.80}Co_{0.15}Al_{0.05}] (OH)_2$ precursors synthesized through hydrothermal method.

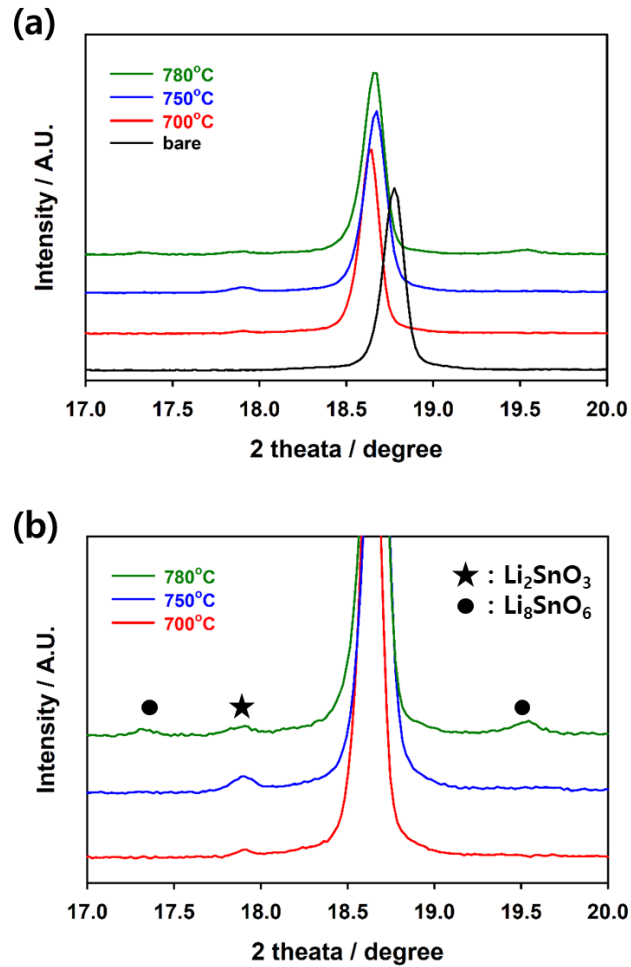


Figure 42. The XRD patterns of Sn 5 at% added

$\text{Li}[\text{Ni}_{0.80}\text{Co}_{0.15}\text{Al}_{0.05}] \text{O}_2$ synthesized at various temperatures.

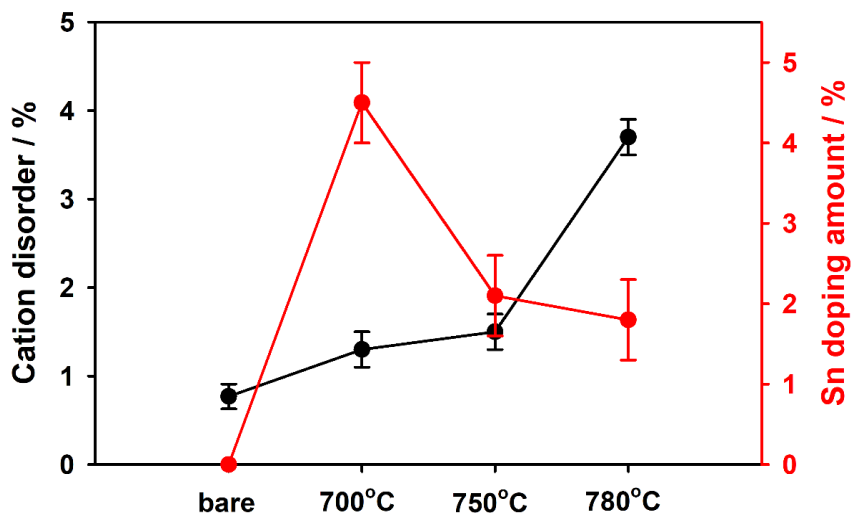


Figure 43. The Rietveld refinement results of XRD patterns in figure 42.

material exhibits higher degree of cation disorder. This is due to the presence of doped Sn^{4+} ion reduces the oxidation state of Ni^{3+} to Ni^{2+} , which easily migrates to Li layer due to similar ionic radius with Li^+ ion. The doping amount of Sn decreases as the heating temperature increases, accompanied with the phase segregation of Li_2SnO_3 . Interestingly, the sharp increase in cation disorder is observed for the sample synthesized at 780°C. This is consistent with the XRD analysis in that Li^+ is dominantly diffused out from host material at 780°C, forming the Li_8SnO_6 . Therefore, it is considered that the optimization synthesis temperature is 750°C for NCA material.

To clarify the phase segregation behavior during synthesis, cross-sectional STEM–EDS mapping analysis was conducted for the sample synthesized at 700 and 750°C. As shown in **figure 44**, Sn is homogenously distributed within the NCA particle synthesized at 700°C. This is consistent with the structural analysis, indicating Sn ions are dominantly doped in the NCA host material. On the other hand, Sn is distributed mainly on the specific surface of the powder synthesized at 750°C. This morphology is similar to the (003) plane-selectively Li_2SnO_3 coated LiCoO_2 , as we have shown in section 3.1. The thickness of the Li_2SnO_3 coating layer is *ca.* 20 nm. (**Figure 45**) To investigate the electrochemical properties of plane-selectively

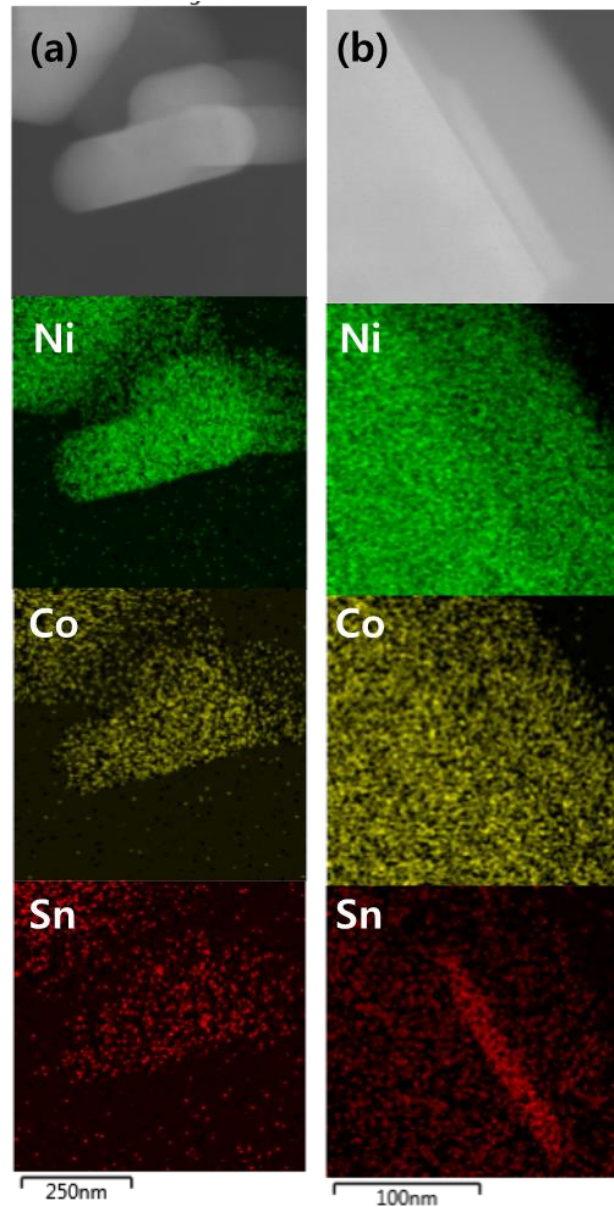


Figure 44. Cross-sectional STEM-EDS mapping images of Sn 5 at% added $\text{Li}[\text{Ni}_{0.80}\text{Co}_{0.15}\text{Al}_{0.05}]\text{O}_2$ synthesized at (a) 700°C and (b) 750°C.

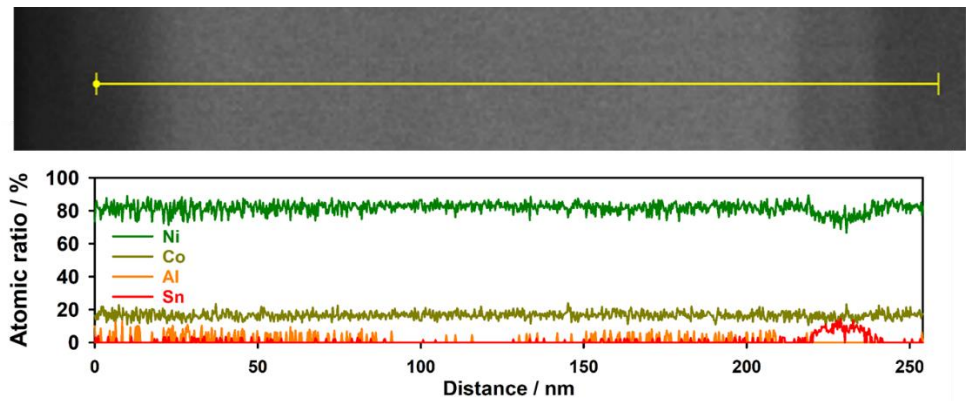


Figure 45. Cross-sectional STEM-EDS line profile of plane-selectively Li_2SnO_3 coated $\text{Li}[\text{Ni}_{0.80}\text{Co}_{0.15}\text{Al}_{0.05}]\text{O}_2$.

Li_2SnO_3 coated NCA material synthesized via hydrothermal synthesis, the rate capability of the bare, conventionally Li_2SnO_3 coated NCA and plane-selectively Li_2SnO_3 coated NCA materials were compared with coin-type half-cells. The bare NCA material was synthesized via hydrothermal method and the conventionally Li_2SnO_3 coated NCA materials was synthesized via sol-gel method which followed the same procedure with the conventional coating of LiCoO_2 . As shown in **figure 46**, the plane-selectively Li_2SnO_3 coated NCA material shows higher discharge capacity at high C rates, *ca.* 2C (400 mA g⁻¹).

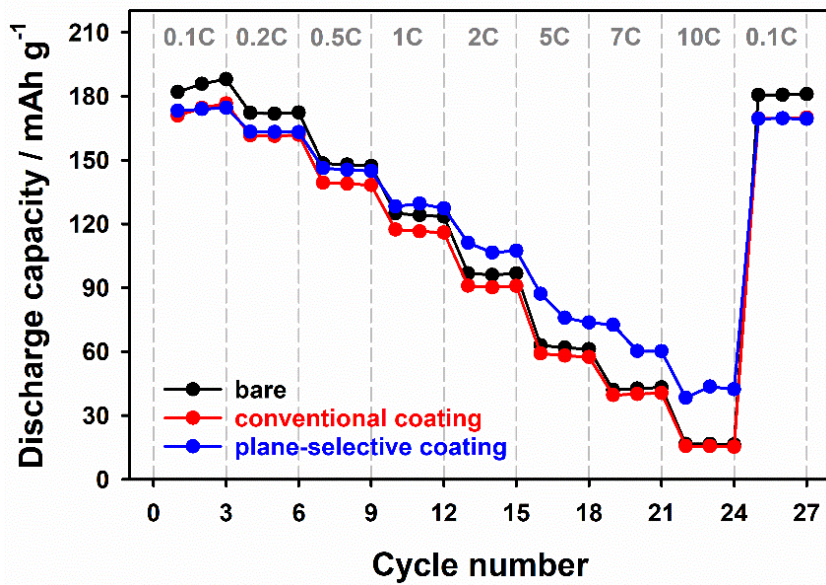


Figure 46. Rate performances of bare, conventionally and plane-selectively Li_2SnO_3 coated $\text{Li}[\text{Ni}_{0.80}\text{Co}_{0.15}\text{Al}_{0.05}]\text{O}_2$.

5. Conclusion

We introduced one-step coating method using the thermal phase segregation of doped materials through the solubility variation of solid solution phases depending on temperatures. Sn was easily doped in layered oxide cathode materials at low temperature (*ca.* 600~700°C), leading to formation of Sn-doped $\text{Li}[\text{Sn}_x\text{TM}_{1-x}]\text{O}_2$ where TM is a combination of Ni, Co, Mn and Al. When the heating temperature is above solubility limit of Sn in host material, the mixture phase of Li_2SnO_3 and the host material is formed due to the excellent thermodynamic stability of Li_2SnO_3 . In particular, Li_2SnO_3 is grown plane-selectively only on (003) surface of LiCoO_2 . This leads to superior rate capability and moderate cycle performance compared with the conventionally coated material.

It is also examined that the application of one-step phase segregation coating method to Ni-rich layered oxide materials such as $\text{Li}[\text{Ni}_{0.8}\text{Co}_{0.1}\text{Mn}_{0.1}]\text{O}_2$ and $\text{Li}[\text{Ni}_{0.80}\text{Co}_{0.15}\text{Al}_{0.05}]\text{O}_2$. It is revealed that presence of Mn^{4+} ions in $\text{Li}[\text{Ni}_{0.8}\text{Co}_{0.1}\text{Mn}_{0.1}]\text{O}_2$ increases the solubility of Sn^{4+} ions in the host material. This results in the increase of heating temperature for phase segregation, which finally leads to degradation of electrochemical properties of the host material.

In contrary to $\text{Li}[\text{Ni}_{0.8}\text{Co}_{0.1}\text{Mn}_{0.1}]\text{O}_2$ active material, the phase segregation of Li_2SnO_3 on Mn-free $\text{Li}[\text{Ni}_{0.80}\text{Co}_{0.15}\text{Al}_{0.05}]\text{O}_2$ occurred at the same temperature at which the temperature of optimized bare $\text{Li}[\text{Ni}_{0.80}\text{Co}_{0.15}\text{Al}_{0.05}]\text{O}_2$ material. With our structural analysis, it was confirmed that no significant structural degradation was occurred in $\text{Li}[\text{Ni}_{0.80}\text{Co}_{0.15}\text{Al}_{0.05}]\text{O}_2$ material. Through the cross-sectional STEM-EDS mapping images, we also found that plane-selective phase segregation is the greatly dependent on the morphology of the host material.

Eventually, by synthesizing $\text{Li}[\text{Ni}_{0.80}\text{Co}_{0.15}\text{Al}_{0.05}]\text{O}_2$ material with plate-like morphology, we could obtain plane-selectively Li_2SnO_3 coated $\text{Li}[\text{Ni}_{0.80}\text{Co}_{0.15}\text{Al}_{0.05}]\text{O}_2$ material. The (003) plane-selectively Li_2SnO_3 coated $\text{Li}[\text{Ni}_{0.80}\text{Co}_{0.15}\text{Al}_{0.05}]\text{O}_2$ material exhibited higher reversible capacity at high C rates (*ca.* 2 C, 400 mA g^{-1}) than bare and the conventionally Li_2SnO_3 coated $\text{Li}[\text{Ni}_{0.80}\text{Co}_{0.15}\text{Al}_{0.05}]\text{O}_2$ material. We believe that this approach is promising for applications demanding excellent high rate performance, such as electric vehicles.

References

1. Ellis, B. L.; Lee, K. T.; Nazar, L. F. *Chem. Mater.* **2010**, *22*, (3), 691–714.
2. Grey, C. P.; Tarascon, J. M. *Nat. Mater.* **2016**, *16*, (1), 45–56.
3. Goodenough, J. B.; Kim, Y. *Chem. Mater.* **2010**, *22*, (3), 587–603.
4. Lu, J.; Chen, Z.; Ma, Z.; Pan, F.; Curtiss, L. A.; Amine, K. *Nat. Nanotechnol.* **2016**, *11*, (12), 1031–1038.
5. Thackeray, M. *Nat. Mater.* **2002**, *1*, (2), 81–82.
6. Liu, H.; Strobridge, F. C.; Borkiewicz, O. J.; Wiaderek, K. M.; Chapman, K. W.; Chupas, P. J.; Grey, C. P. *Science* **2014**, *344*, (6191), 1252817.
7. Schipper, F.; Erickson, E. M.; Erk, C.; Shin, J.-Y.; Chesneau, F. F.; Aurbach, D. *J. Electrochem. Soc.* **2017**, *164*, (1), A6220–A6228.
8. Thackeray, M. M.; Kang, S.-H.; Johnson, C. S.; Vaughey, J. T.; Benedek, R.; Hackney, S. A. *J. Mater. Chem.* **2007**, *17*, (30), 3112.
9. Zhang, X.; Lengyel, M.; Axelbaum, R. L. *AIChE J.* **2014**, *60*, (2), 443–450.
10. Grimaud, A.; Hong, W. T.; Shao-Horn, Y.; Tarascon, J. M. *Nat. Mater.* **2016**, *15*, (2), 121–6.
11. Noh, H.-J.; Youn, S.; Yoon, C. S.; Sun, Y.-K. *J. Power Sources*

- 2013, 233, 121–130.
12. Fell, C. R.; Carroll, K. J.; Chi, M.; Meng, Y. S. *J. Electrochem. Soc.* 2010, 157, (11), A1202–A1211.
13. Xu, B.; Qian, D.; Wang, Z.; Meng, Y. S. *Mater. Sci. Eng. R Rep.* 2012, 73, (5–6), 51–65.
14. Myung, S. T.; Noh, H. J.; Yoon, S. J.; Lee, E. J.; Sun, Y. K. *J. Phys. Chem. Lett.* 2014, 5, (4), 671–9.
15. Li, Y.; Lu, Y.; Adelhelm, P.; Titirici, M.-M.; Hu, Y.-S. *Chem. Soc. Rev.* 2019, 48, (17), 4655–4687.
16. Kim, Y.; Kim, D. S.; Um, J. H.; Yoon, J.; Kim, J. M.; Kim, H.; Yoon, W.-S. *ACS Appl. Mater. Interfaces* 2018, 10, (35), 29992–29999.
17. Park, J.-H.; Kim, J.-M.; Lee, C. K.; Lee, S.-Y. *J. Power Sources* 2014, 263, 209–216.
18. Markevich, E.; Salitra, G.; Hartmann, P.; Kulisch, J.; Aurbach, D.; Park, K.-J.; Yoon, C. S.; Sun, Y.-K. *2019*, 166, (3), A5265–A5274.
19. Park, K.-J.; Hwang, J.-Y.; Ryu, H.-H.; Maglia, F.; Kim, S.-J.; Lamp, P.; Yoon, C. S.; Sun, Y.-K. *ACS Energy Letters* 2019, 4, (6), 1394–1400.
20. Li, W.; Dolocan, A.; Oh, P.; Celio, H.; Park, S.; Cho, J.; Manthiram, A. *Nat. Commun.* 2017, 8, 14589.
21. Zhou, A.; Liu, Q.; Wang, Y.; Wang, W.; Yao, X.; Hu, W.; Zhang, L.;

- Yu, X.; Li, J.; Li, H. *J. Mater. Chem. A* **2017**, 5, (46), 24361–24370.
22. Lee, S.-H.; Yoon, C. S.; Amine, K.; Sun, Y.-K. *J. Power Sources* **2013**, 234, 201–207.
23. Jo, C.-H.; Cho, D.-H.; Noh, H.-J.; Yashiro, H.; Sun, Y.-K.; Myung, S. T. *Nano Research* **2014**, 8, (5), 1464–1479.
24. You, Y.; Celio, H.; Li, J.; Dolocan, A.; Manthiram, A. *Angew. Chem. Int. Ed.* **2018**, 57, (22), 6480–6485.
25. Cho, Y.; Eom, J.; Cho, J. *J. Electrochem. Soc.* **2010**, 157, (5), A617–A624.
26. Dahalon, L.; Dedryvère, R.; Martinez, H.; Flahaut, D.; Ménétrier, M.; Delmas, C.; Gonbeau, D. *Chem. Mater.* **2009**, 21, (23), 5607–5616.
27. Kalluri, S.; Yoon, M.; Jo, M.; Liu, H. K.; Dou, S. X.; Cho, J.; Guo, Z. *Adv. Mater.* **2017**, 29, (48).
28. Padhi, A. K.; Nanjundaswamy, K. S.; Goodenough, J. B. *J. Electrochem. Soc.* **1997**, 144, (4), 1188–1194.
29. Yamada, A.; Chung, S. C.; Hinokuma, K. *J. Electrochem. Soc.* **2001**, 148, (3), A224.
30. Andersson, A. S. *Electrochem. and Solid-State Lett.* **1999**, 3, (2), 66.
31. Castro, L.; Dedryvère, R.; El Khalifi, M.; Lippens, P. E.; Bréger,

- J.; Tessier, C.; Gonbeau, D. *J. Phys. Chem. C* **2010**, *114*, (41), 17995–18000.
32. Tang, P.; Holzwarth, N. A. W. *Phys. Rev. B* **2003**, *68*, (16), 165107.
33. Kong, W.; Li, H.; Huang, X.; Chen, L. *J. Power Sources* **2005**, *142*, (1–2), 285–291.
34. Kim, Y. *J. Solid State Electrochem.* **2013**, *17*, (7), 1961–1965.
35. Liu, X.; Wang, Y. J.; Barbiellini, B.; Hafiz, H.; Basak, S.; Liu, J.; Richardson, T.; Shu, G.; Chou, F.; Weng, T. C.; Nordlund, D.; Sokaras, D.; Moritz, B.; Devereaux, T. P.; Qiao, R.; Chuang, Y. D.; Bansil, A.; Hussain, Z.; Yang, W. *Phys. Chem. Chem. Phys.* **2015**, *17*, (39), 26369–77.
36. Thackeray, M. M.; Johnson, P. J.; de Picciotto, L. A.; Bruce, P. G.; Goodenough, J. B. *Mater. Res. Bull.* **1984**, *19*, (2), 179–187.
37. Shaju, K. M.; Bruce, P. G. *Chem. Mater.* **2008**, *20*, (17), 5557–5562.
38. Choi, N.-S.; Yeon, J.-T.; Lee, Y.-W.; Han, J.-G.; Lee, K. T.; Kim, S.-S. *Solid State Ion.* **2012**, *219*, 41–48.
39. Zhou, G.; Sun, X.; Li, Q.-H.; Wang, X.; Zhang, J.-N.; Yang, W.; Yu, X.; Xiao, R.; Li, H. *J. Phys. Chem. Lett.* **2020**, *11*, (8), 3051–3057.
40. Shin, H.; Park, J.; Sastry, A. M.; Lu, W. *J. Power Sources* **2015**,

284, 416–427.

41. Zhan, C.; Lu, J.; Jeremy Kropf, A.; Wu, T.; Jansen, A. N.; Sun, Y.-K.; Qiu, X.; Amine, K. *Nat. Commun.* **2013**, 4, (1), 2437.
42. Choi, N.-S.; Han, J.-G.; Ha, S.-Y.; Park, I.; Back, C.-K. *RSC Advances* **2015**, 5, (4), 2732–2748.
43. Ohzuku, T.; Ueda, A.; Nagayama, M.; Iwakoshi, Y.; Komori, H. *Electrochim. Acta* **1993**, 38, (9), 1159–1167.
44. Ohzuku, T.; Ueda, A. *J. Electrochem. Soc.* **1994**, 141, (11), 2972–2977.
45. Yano, A.; Shikano, M.; Ueda, A.; Sakaebi, H.; Ogumi, Z. *J. Electrochem. Soc.* **2017**, 164, (1), A6116–A6122.
46. Gong, Y.; Zhang, J.; Jiang, L.; Shi, J. A.; Zhang, Q.; Yang, Z.; Zou, D.; Wang, J.; Yu, X.; Xiao, R.; Hu, Y. S.; Gu, L.; Li, H.; Chen, L. *J. Am. Chem. Soc.* **2017**, 139, (12), 4274–4277.
47. Duffiet, M.; Blangero, M.; Cabelguen, P.-E.; Delmas, C.; Carlier, D. *J. Phys. Chem. Lett.* **2018**, 9, (18), 5334–5338.
48. Wang, L.; Chen, B.; Ma, J.; Cui, G.; Chen, L. *Chem. Soc. Rev.* **2018**, 47, (17), 6505–6602.
49. Venkatraman, S.; Shin, Y.; Manthiram, A. *Electrochem. Solid-State Lett.* **2003**, 6, (1), A9.
50. Manthiram, A.; Vadivel Murugan, A.; Sarkar, A.; Muraliganth, T.

- Energy Environ. Sci.* **2008**, 1, (6), 621.
51. Amatucci, G. G.; Tarascon, J. M.; Klein, L. C. *Solid State Ion.* **1996**, 83, (1), 167–173.
52. Arroyo y de Dompablo, M. E.; Ceder, G. *J. Power Sources* **2003**, 119–121, 654–657.
53. Kalyani, P.; Kalaiselvi, N. *Sci. Technol. Adv. Mater.* **2016**, 6, (6), 689–703.
54. Takahashi, Y.; Akimoto, J.; Gotoh, Y.; Kawaguchi, K.; Mizuta, S. *J. Solid State Chem.* **2001**, 160, (1), 178–183.
55. Dahn, J. R.; von Sacken, U.; Michal, C. A. *Solid State Ion.* **1990**, 44, (1), 87–97.
56. Manthiram, A. *Nat. Commun.* **2020**, 11, (1), 1550.
57. Gilbert, J. A.; Shkrob, I. A.; Abraham, D. P. *J. Electrochem. Soc.* **2017**, 164, (2), A389–A399.
58. Jung, R.; Linsenmann, F.; Thomas, R.; Wandt, J.; Solchenbach, S.; Maglia, F.; Stinner, C.; Tromp, M.; Gasteiger, H. A. *J. Electrochem. Soc.* **2019**, 166, (2), A378–A389.
59. Yang, H.; Zhuang, G. V.; Ross, P. N. *J. Power Sources* **2006**, 161, (1), 573–579.
60. Jung, S.-K.; Gwon, H.; Hong, J.; Park, K.-Y.; Seo, D.-H.; Kim, H.; Hyun, J.; Yang, W.; Kang, K. *Adv. Energy Mater.* **2014**, 4, (1),

1300787.

61. Yoon, W.-S.; Balasubramanian, M.; Chung, K. Y.; Yang, X.-Q.; McBreen, J.; Grey, C. P.; Fischer, D. A. *J. Am. Chem. Soc.* **2005**, 127, (49), 17479–17487.
62. Hall, D. S.; Self, J.; Dahn, J. R. *J. Phys. Chem. C* **2015**, 119, (39), 22322–22330.
63. Shakourian-Fard, M.; Kamath, G.; Sankaranarayanan, S. K. *Chemphyschem* **2016**, 17, (18), 2916–30.
64. Zhan, C.; Wu, T.; Lu, J.; Amine, K. *Energy Environ. Sci.* **2018**, 11, (2), 243–257.
65. Wang, H.; Rus, E.; Sakuraba, T.; Kikuchi, J.; Kiya, Y.; Abruna, H. D. *Anal. Chem.* **2014**, 86, (13), 6197–201.
66. Xu, S.; Luo, G.; Jacobs, R.; Fang, S.; Mahanthappa, M. K.; Hamers, R. J.; Morgan, D. *ACS Appl. Mater. Interfaces* **2017**, 9, (24), 20545–20553.
67. Oh, S.; Lee, J. K.; Byun, D.; Cho, W. I.; Won Cho, B. *J. Power Sources* **2004**, 132, (1–2), 249–255.
68. Scott, I. D.; Jung, Y. S.; Cavanagh, A. S.; Yan, Y.; Dillon, A. C.; George, S. M.; Lee, S. H. *Nano Lett.* **2011**, 11, (2), 414–8.
69. Araki, K.; Taguchi, N.; Sakaebé, H.; Tatsumi, K.; Ogumi, Z. *J. Power Sources* **2014**, 269, 236–243.

70. Dai, X.; Zhou, A.; Xu, J.; Yang, B.; Wang, L.; Li, J. *J. Power Sources* **2015**, *298*, 114–122.
71. Woo, S.-G.; Han, J.-H.; Kim, K. J.; Kim, J.-H.; Yu, J.-S.; Kim, Y.-J. *Electrochim. Acta* **2015**, *153*, 115–121.
72. Xu, Y.; Li, X.; Wang, Z.; Guo, H.; Huang, B. *Mater. Lett.* **2015**, *143*, 151–154.
73. Lee, J.-G.; Kim, B.; Cho, J.; Kim, Y.-W.; Park, B. *J. Electrochem. Soc.* **2004**, *151*, (6), A801–A805.
74. Cho, J.; Kim, T.-G.; Kim, C.; Lee, J.-G.; Kim, Y.-W.; Park, B. *J. Power Sources* **2005**, *146*, (1–2), 58–64.
75. Sun, Y.-K.; Yoon, C. S.; Myung, S.-T.; Belharouak, I.; Amine, K. *J. Electrochem. Soc.* **2009**, *156*, (12), A1005–A1010.
76. Tron, A.; Park, Y. D.; Mun, J. *J. Power Sources* **2016**, *325*, 360–364.
77. Song, H. G.; Kim, S. B.; Park, Y. J. *J. Electroceram.* **2012**, *29*, (2), 163–169.
78. Bai, Y.; Jiang, K.; Sun, S.; Wu, Q.; Lu, X.; Wan, N. *Electrochim. Acta* **2014**, *134*, 347–354.
79. Kim, Y. J.; Cho, J.; Kim, T.-J.; Park, B. *J. Electrochem. Soc.* **2003**, *150*, (12), A1723–A1725.
80. Lee, D.-J.; Scrosati, B.; Sun, Y.-K. *J. Power Sources* **2011**, *196*,

- (18), 7742–7746.
81. Min, S. H.; Jo, M. R.; Choi, S.-Y.; Kim, Y.-I.; Kang, Y.-M. *Adv. Energy Mater.* **2016**, 6, (7), 1501717.
82. Cho, Y.; Cho, J. *J. Electrochem. Soc.* **2010**, 157, (6), A625.
83. Jung, Y. S.; Cavanagh, A. S.; Dillon, A. C.; Groner, M. D.; George, S. M.; Lee, S.-H. *J. Electrochem. Soc.* **2010**, 157, (1), A75–A81.
84. Shi, Y.; Zhang, M.; Qian, D.; Meng, Y. S. *Electrochim. Acta* **2016**, 203, (Supplement C), 154–161.
85. Kramer, D.; Ceder, G. *Chem. Mater.* **2009**, 21, (16), 3799–3809.
86. Hu, L.; Xiong, Z.; Ouyang, C.; Shi, S.; Ji, Y.; Lei, M.; Wang, Z.; Li, H.; Huang, X.; Chen, L. *Phys. Rev. B* **2005**, 71, (12).
87. Bianchini, M.; Fauth, F.; Hartmann, P.; Brezesinski, T.; Janek, J. *J. Mater. Chem. A* **2020**, 8, (4), 1808–1820.
88. Koyama, Y.; Arai, H.; Tanaka, I.; Uchimoto, Y.; Ogumi, Z. *J. Mater. Chem. A* **2014**, 2, (29), 11235–11245.

국문 초록

상 분리를 통한 리튬이온 전지용 층상계 산화물 양극

소재 표면 개질

김 한 슬

서울대학교 대학원

화학생물공학부

고전압에서 구동되는 양극 활물질의 표면에서 발생하는 전해질 분해, 전이 금속 용해 등의 비가역적인 부반응은 리튬 이온 전지 열화에 큰 영향을 미친다. 따라서, 리튬 이온 전지용 양극 활물질의 성능 향상에 있어 표면 개질 기술의 중요성이 점점 더 증가하고 있다. 이를 해결하기 위해, 양극 활물질 계면의 안정성을 증대시키기 위해 다양한 방법의 코팅 기술이 개발되었다. 산화물, 인산화물, 불화물 등을 코팅 소재로 사용하는 기존의 코팅 방법은 코팅 층의 균일도와 두께 조절에만 집중하고 있다. 하지만, 건식 코팅법, 습식 코팅법, 원자 충 충착법 등의 기존의 코팅법을 통해 형성된 코팅층은 리튬 이온이 삽입/탈리되는 면을 포함한 방향을 코팅함으로써 전하 전달 저항의 증가를 유발한다. 이러한 점은 양극 활물질의 출력 특성을 저하시킴으로써, 고율에서의 사용을

필요로 하는 전기 자동차 등의 사용에 걸림돌이 되고 있다.

본 연구에서는 온도에 따른 Sn의 용해도 변화를 이용해 Sn이 도핑된 충상계 산화물 양극 소재와 Li_2SnO_3 간의 상분리 현상을 이용한 Li_2SnO_3 에피택셜한 코팅법을 소개한다. 단결정 LiCoO_2 의 경우, 단일 합성 단계를 통해 (003) 면 선택적으로 Li_2SnO_3 가 코팅된 LiCoO_2 를 합성했다. 또한, 다양한 조성의 충상계 산화물 소재에서의 상분리 현상 관찰을 통해, Ni-rich 충상계 산화물에의 면 선택적 코팅법 적용에 필수적인 요소들을 밝혀내었다. 망간 이온이 포함된 Ni-rich $\text{Li}[\text{Ni}_{0.8}\text{Co}_{0.1}\text{Mn}_{0.1}]\text{O}_2$ 소재에서는 Mn^{4+} 이온의 존재로 인해 Sn^{4+} 이온의 용해도가 증가하여, 상분리가 발생하는 온도에서 활물질의 열화가 발생한다. 이에 반해, 망간 이온이 없는 Ni-rich $\text{Li}[\text{Ni}_{0.80}\text{Co}_{0.15}\text{Al}_{0.05}]\text{O}_2$ 소재에서는 상분리로 인한 활물질의 열화가 없음을 밝혀냈다. 하지만, Ni-rich 소재의 무작위한 입자 형태로 인해 면선택적 코팅이 일어나지 않음을 알아내었다. 이를 개선하기 위해, 수열 합성법을 통해 plate-like 입자 형태를 가지는 $\text{Li}[\text{Ni}_{0.80}\text{Co}_{0.15}\text{Al}_{0.05}]\text{O}_2$ 소재를 합성함으로써, (003) 면 선택적으로 Li_2SnO_3 코팅된 Ni-rich $\text{Li}[\text{Ni}_{0.80}\text{Co}_{0.15}\text{Al}_{0.05}]\text{O}_2$ 소재를 합성하였다. (003) 면 선택적으로 Li_2SnO_3 코팅된 충상계 산화물 양극 소재는 리튬 이온 전하 전달 저항을 증가시키는 저항층이 없다. 이로 인해, (003) 면 선택적 Li_2SnO_3 코팅된 충상계 양극 소재는 기존의 코팅법으로 코팅된 소재에 비해 우수한 출력 특성을 보이며, 이는

고율에서의 구동이 필요한 배터리 소재에 대한 유망한 코팅법으로 생각된다.

키워드 : 리튬 이온 전지, 양극 소재, 면 선택적, 에피택셜, 상 분리

학번 : 2016-30230

